

POLITECNICO DI TORINO

a.a. 2019/2020

Corso di laurea Magistrale in Ingegneria Civile

PROVA FINALE

Identification of elastic material parameters
from experimental kinematic fields



Relatore dal Politecnico di Torino:

Prof. Alberto Cina.

Relatori da Université Grenoble Alpes:

Prof. Gioacchino Viggiani, Ing. Olga Stamati, Ing. Edward Andò, Prof.
Emmanuel Roubin.

Allieva:

Chiara Rossi

Abstract

The aim of this thesis is to find the mechanical properties of a non-homogeneous material in the hypothesis of elastic behaviour.

To overcome the problems of conventional testing, in which the macroscopic properties are determined, and identify the real Poisson's ratio of a material, the spatial distribution of displacements has been measured. To obtain, what is called, a displacement field, Digital Image Correlation (DVC), is used. Thanks to the DVC it has been possible to obtain displacement field measurements from a 3D image series (from initial to deformed), results of a test.

The 3D images treated in this thesis are either synthetically generated, or as a result of x-ray tomography on a real experiment.

In both cases the initial configuration of the specimens has been chosen with increasingly complicated morphologies. Starting from the homogeneous configuration, up to a specimen with many void spherical defects.

In the synthetic case, once the image of the initial configuration is generated, it is deformed with a displacement field resulting from a Finite Element simulation.

In the case where the campaign of experiments is carried out once the material has been chosen with the desired configuration, the images are obtained thanks to in-situ tomography, combining x-ray tomography and uniaxial compression testing. Once the images are generated, these are correlated to produce the *real* displacement field, from which the boundary conditions are extracted.

The boundary conditions are then applied in Finite Element simulations. The FE meshes are representative of the initial configuration of the material. In the simulation the linear elastic behaviour is assumed, and in each of them different values are chosen for the elastic constants of the material (output of the treatment). The result of each simulation is a *simulated* displacement field.

By searching which *simulated* displacement field is the most similar to the *real* displacement field it has been possible to identify Poisson's ratio of the material tested.

(315 words)

Contents

1	Introduction	1
2	Theoretical background: Constitutive laws	3
3	Tools	6
3.1	X-ray tomography	6
3.2	Digital Image Correlation	7
3.3	Finite Element simulation	9
3.4	Equilibrium Gap Method, EGM	11
4	Simulated kinematic fields	12
4.1	Methodology, Homogeneous case	13
4.1.1	Step 1: Specimen Generation	13
4.1.2	Step 2: Deformed configuration	15
4.1.3	Step 3: Local Digital Volume Correlation, Extracting the boundary conditions	18
4.1.4	Inter Step: reference residual field	20
4.1.5	Step 4: Identification of elastic parameters	23
4.2	Case with a large void spherical defect	26
4.3	Case with many void spherical defects	32
4.3.1	Difference between working on the complete specimen and cropping around a single sphere	32
4.3.2	Big number of defects	33
5	Experimental kinematic fields	35
5.0.1	Material	35
5.0.2	In-situ experiments	36
5.1	Step 3: Local Digital Image Correlation, Extracting the boundary conditions . . .	40
5.2	Step 4: Identification of elastic parameters	42
5.2.1	NPH	42
5.2.2	Noodle foam, heterogeneous, Sponge	42
6	Conclusions and Perspectives	43

List of Figures

1	Vertical cut of images, from initial configuration, deformed configuration and displacement field (in px) in the z direction result of the DVC.	1
2	Infinitesimal strains, (Lancellotta, 1995).	3
3	Schematic representation of the stress-strain diagram, linear elastic behaviour , (Lancellotta, 1995).	4
4	(a) Principle of tomography; (b) Synchrotron and laboratory tomograph. (from [Salvo et al. 2010]	6
5	In-situ x-ray facility at Laboratoire 3SR.	7
6	Representative vertical slices and greylevel histograms of the corresponding reconstructed 3D volumes for a uniaxial tension.	9
7	Representative vertical slices and greylevel histograms of the corresponding reconstructed 3D volumes for a uniaxial tension.	10
8	Unstructured 3D mesh made of 4-node tetrahedra, and FE mesh which represents the initial configuration of the material.	11
9	Project flowchart for identification of elastic material parameters from simulated kinematic fields.	12
10	Project flowchart for Specimen generation.	13
11	cube, l = 141 mm, central cut, No Texture.	13
12	cube, l = 141 mm, central cut, No Texture, lc = 3-5-10 mm	14
13	cube, l = 141 mm, central cut, lc = 3 mm, SNR = 10 and SNR = 40	15
14	Project flowchart for Deformed configuration generation.	15
15	cube, l = 141 mm, central cut, lchar = 3 mm, lchar = 5 mm, lchar = 7 mm, lchar = 10 mm.	16
16	Axial displacement field in a FE mesh with lchar = 5 mm, applied displacement: 3 mm in z direction in z = 141 mm.	17
17	Deformed configuration as image, lchar = 3-5-7-10 mm, applied displacement: 3 mm in z direction in z = 141 mm	17
18	Project flowchart for Extracting the boundary conditions.	18
19	Results from LDIC, return status, lc = 3 mm, lchar = 3 mm, hws = 3, 7 and 14.	18
20	Results from LDIC, lc = 3 mm, lchar = 3 mm, axial displacement field, hws = 3, 7 and 14 mm.	19
21	Axial displacement field from DVC interpolated using the mesh, lc = 3 mm, lchar = 3 mm, hws = 3, 7 and 14.	19
22	Boundary Condition, lc = 3 mm, lchar = 3 mm, hws = 7 mm.	20
23	Simulated displacement field, lc = 3 mm, lchar = 3 mm, hws = 3, 7 and 14 mm.	20
24	Displacement residual, direction z, cube, l = 141 mm, central cut, lc = 3 mm, lchar = 3 mm, hws = 3, 7 and 14 mm.	21
25	Displacement residual, direction z, cube l = 141 mm, central cut, lc = 10 mm, lchar = 10 mm, hws = 3, 7 and 14 mm.	21
26	Error, cube, l = 141 mm, No Noise, lc = 3, 5 and 10 mm, lchar = 3, 5, 7 and 10 mm, hws = 3, 7 and 14 mm.	22
27	Error, cube, l = 141 mm, With Noise, lc = 3, 5 mm, lchar = 3, 7 mm, hws = 3, 7 and 14 mm, SNR = 10, 20, 30, 40 (a). Error, cube, l = 141 mm, With Noise, lc = 3 mm, lchar = 3 mm, hws = 3, 7 and 14 mm, SNR = 2, 4, 6, 8, 10, 20, 30, 40 (b).	23
28	Project flowchart for the identification.	23
29	Identification homogeneous material, traction.	24
30	Homogeneous cases, different types of load and sample size.	25
31	Identification homogeneous cases, different types of load and sample size.	26
32	Cases with central sphere, l = 400 mm, lc = 3 mm, radius = 20, 50, 100 mm.	27
33	Macroscopic stress-strain response radius = 90, 100, 120 mm, lchar = 5, 6, 10, 15 mm.	27
34	Difference in representation of a sphere of radius 40 mm between a mesh with lchar = 6 mm and lchar = 15 mm.	28
35	Cases with central sphere, l = 400 mm, lc = 3 mm, radius = 20, 50, 100 mm, lchar = 7 mm, deformed configuration.	28

36	Cases with central sphere, $l = 400$ mm, $lc = 3$ mm, radius = 100 mm, $lchar = 7$ mm, $hws = 7$ mm, return status and displacement in z direction from the DVC (b), displacement in z direction corrected (c).	29
37	Interpolated DVC, cases with central sphere, $l = 400$ mm, $lc = 3$ mm, radius = 100 mm, $lchar = 7$ mm, $hws = 7$ mm, displacement in z direction from the DVC corrected and interpolated.	29
38	Cases with central sphere, $l = 400$ mm, $lc = 3$ mm, radius = 100 mm, $lchar = 7$ mm, $hws = 7$ mm, displacement in z direction from the simulated displacement field.	30
39	Cases with central sphere, $l = 400$ mm, $lc = 3$ mm, radius = 100 mm, $lchar = 7$ mm, $hws = 7$ mm, residual field.	30
40	Cases with central sphere, $l = 400$ mm, $lc = 3$ mm, radius = 100 mm, $lchar = 7$ mm, $hws = 7$ mm, minimisation of the error.	31
41	Cases with 6 spheres, $l = 400$ mm, radius = 20 mm, $lchar = 7$ mm, $hws = 7$ mm, initial configuration, whole sample and cutout around a sphere.	32
42	Cases with 6 spheres, $l = 400$ mm, radius = 20 mm, $lchar = 7$ mm, $hws = 7$ mm, minimisation of the error.	32
43	Cases with big number of defects, $l = 400$ mm, radius = 30 mm.	33
44	Cases with big number of defects, $l = 400$ mm, radius = 30 mm, parametric analysis.	33
45	Cases with big number of defects, $l = 400$ mm, radius = 30/50/100 mm, minimisation of the error.	34
46	Noodle foam, Sample 1, 2 and 3, respectively, homogeneous, with defect, with defect and bad boundary conditions.	35
47	Sponge sample.	36
48	Noodle foam, Sample 1 macroscopic force-displacement curve.	36
49	Noodle foam, Sample 2 macroscopic force-displacement curve.	37
50	Noodle foam, Sample 3 macroscopic force-displacement curve.	37
51	Sponge, macroscopic force-displacement curve.	38
52	Central horizontal and vertical slices of the reconstructed 3D images of the SCAN 1, Noodle foam, respectively, NFH, NFD, NFDBC.	39
53	Central vertical slices of the reconstructed 3D images of the SCAN 1, Sponge.	40
54	NFH, results from LDIC Scan2-Scan3, axial displacement field, $hws = 25$ px.	40
55	NFD, results from LDIC Scan1-Scan2, return status, $hws = 25$ px.	41
56	NPH, mesh of the initial configuration, and DVC interpolated in the mesh.	41
57	NPH axial displacement field DVC interpolated in the mesh, axial displacement field simulated, residual z direction.	42
58	NPH, minimisation of the error.	42

List of Tables

1	Identification homogeneous material, traction.	24
2	Identification homogeneous, material, different types of load and sample size.	26
3	Identification case with a large void spherical defect.	31
4	Identification case many void spherical defect, complete specimen and cropping around a single sphere.	32
5	Identification case many void spherical defect, different spheres size.	34

1 Introduction

In civil engineering, the security of knowing the materials used, their behaviour and their parameters is extremely important.

Over the years many mathematical models have been created, in order to describe the materials, the models are derived from experimental data, and they divide the materials into classes of behaviour. Each model idealizes, more or less, a real behaviour of a studied material.

Each class has its own law that describes the behaviour, one material in particular is specify according to the constants that are present in the law, more the function is mathematically complex greater is the number of constants, if the law is a straight line there are only two parameters that specify the material.

Therefore, if is assumed to know a priori in which of these models a material belongs, only the constants of the law must be defined. These are determined by experimental tests.

Conventional material testing, are global processes that are only able to extract the average response of the material. In this kind of test results are global data with no information between measurement points, therefore, in the case of non-homogeneous material or processes, the information that characterize the heterogeneity and the state of the boundary conditions are lost. [Viggiani and Hall 2008, Grediac 2004]

Without the certainty that the material is perfectly homogeneous, as well as the instrumentation for the test, the parameters that are derived from this test are not precisely the parameters of the material studied.

In recent years more innovative techniques have been developed that allow to obtain, not global measurements, but field records of a quantity, which are called Full-field measurements. Not only do they have the ability to best manage anisotropic and heterogeneity, they also have the advantage of being non-contact techniques.

In order to study the behaviour of materials it is standard to have the measurement of deformations as a function of an applied stress. In full field measurements, this translates into the measurement of displacement field from field measurements taken of samples deforming. In this case the measurements of the deformation fields (Figure 1 c) are obtained using the Digital Image Correlation between the 3D image of the initial and final configuration. These 3D images are produced with tests, performed inside the x-ray tomograph (Figure 1 a and b) or from the simulations of mechanical tests.

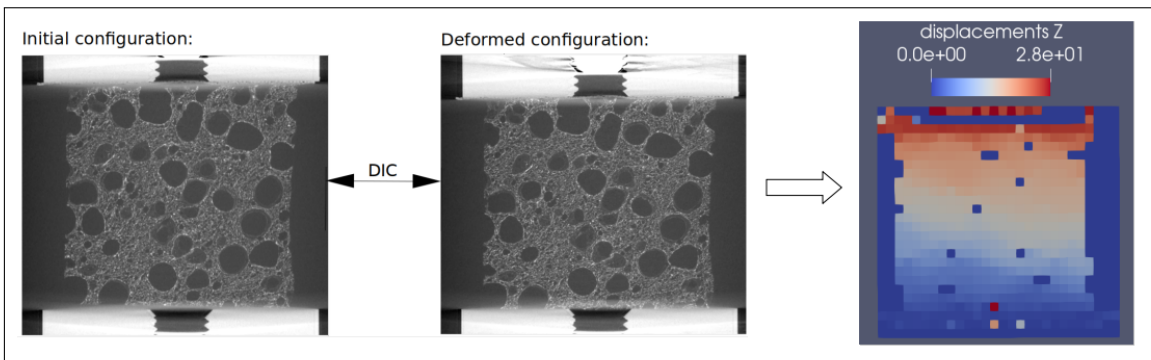


Figure 1: Vertical cut of images, from initial configuration, deformed configuration and displacement field (in px) in the z direction result of the DVC.

To find the parameters of a constitutive law, full field measurements are embedded with finite element simulations.[Grediac 2004]

In this work the simulations aim for an output (simulated displacement field) that is as close to reality (real displacement field from the DVC) as possible so that the parameters used in the simulation are also the parameters of the real material.

To generate the mesh that is simulated, the initial sample configuration, visible in Figure 1a, is projected in a generic mesh with tetrahedral elements. In order to simulate the actual test to which the specimen has been subjected, the boundary conditions derived from the real displacement field (result of the DVC) are imposed in the procedure.

In particular is searched one of the two elastic parameters (Poisson's ratio) that gives shape to the linear elastic constitutive law.

To complete the procedure described, two different approaches can be used, both developed in this thesis.

The first approach involves starting with an experimental campaign: using an x-ray in-situ mechanical test is possible to obtain 3D images in sequence showing how the specimen deforms with increasing load (corresponding to a compression test). Since the behaviour of the material is supposed to be linear elastic to obtain representative parameters, it is not necessary to have different load steps, in fact it is sufficient the last deformed configuration that corresponds to the total load. At the end of the load test, two 3D images are realized, the first in initial configuration and the second in deformed configuration. Both images are characterized by a certain texture (function of the material and observation scale) and by a noise, due to the instrumentation used.

The second method has a more theoretical approach. It involves the generation of an image (3D) that is representative of an elastic material with defects in it. Since this is a simulated image it is possible to control and compare many of the parameters that affect the accuracy of the final results. As in the experimental case also in this approach, it is necessary to obtain a deformed image. This is done starting the initial configuration, simulating the mechanical test, which deformed the specimen, with finite element simulations are used.

2 Theoretical background: Constitutive laws

Real materials have a discrete nature, but at an engineering level mathematical models require that they are studied through the mechanics of continuous bodies, macroscopic physical systems in which the size of the observed phenomena is such that it is not effects of the molecular structure of matter and for which it is assumed that matter is uniformly distributed and that it fills the space that the body occupies.[Lancellotta 2008]

The language of continuous mechanics is based on the tensor notation in which it is possible to define mathematical entities of the second order that represent deformations and stresses. The tensor of deformations is defined starting from the infinitesimal strains, shown in Figure 2 in the x,y plane.

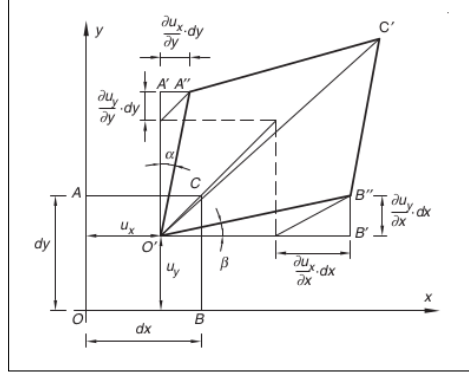


Figure 2: Infinitesimal strains, (Lancellotta, 1995).

- Longitudinal strain:

$$\epsilon_{11} = \epsilon_{xx} = \frac{\delta u_x}{\delta x}, \quad \epsilon_{22} = \epsilon_{yy} = \frac{\delta u_y}{\delta y}, \quad (1)$$

$$\epsilon_{33} = \epsilon_{zz} = \frac{\delta u_z}{\delta z} \quad (2)$$

- Shear strain:

$$\epsilon_{12} = \epsilon_{21} = \gamma_{xy} = \frac{\delta u_x}{\delta y} + \frac{\delta u_y}{\delta x}, \quad \epsilon_{13} = \epsilon_{31} = \gamma_{xz} = \frac{\delta u_x}{\delta z} + \frac{\delta u_z}{\delta x} \quad (3)$$

$$\epsilon_{23} = \epsilon_{32} = \gamma_{zy} = \frac{\delta u_z}{\delta y} + \frac{\delta u_y}{\delta z} \quad (4)$$

$$[\epsilon_{ij}] = \begin{bmatrix} \epsilon_{11} & \epsilon_{12} & \epsilon_{13} \\ \epsilon_{21} & \epsilon_{22} & \epsilon_{23} \\ \epsilon_{31} & \epsilon_{32} & \epsilon_{33} \end{bmatrix} \quad (5)$$

The stress tensor is a linear mapping that associates to each unit normal n the traction vector t , acting on the surface of outward normal n , the diagonal components act normal to the coordinate planes and are called normal stresses, while the off-diagonal components act tangential to the coordinate planes and are called shear stresses.

$$[\sigma_{ij}] = \begin{bmatrix} \sigma_{11} & \sigma_{12} & \sigma_{13} \\ \sigma_{21} & \sigma_{22} & \sigma_{23} \\ \sigma_{31} & \sigma_{32} & \sigma_{33} \end{bmatrix} \quad (6)$$

The behaviour of materials is strictly dependent on their constitution and is made explicit by the constitutive laws with which it is possible to predict the response of a deformable medium subject to load histories that are not necessarily simple.

In particular in this work the hypothesis of linear elastic behaviour is accepted as valid for the materials studied. This leads to a very simple constitutive law and also gives the possibility to

have a solution in closed form.

An ideal solid is defined elastic if in any phase of unloaded loading, its response is characterized by a biunivocal correspondence between tensions and deformations.

Consequently, all the work spent during the deformation is completely returned once the disturbing cause is removed.

Introducing the hypothesis of linear bond, schematization in Figure 3, of initial unformed state and null tensional state in the absence of deformations, it is possible to obtain the following constitutive law:

$$[\sigma_{ij}] = D_{ijhk}\epsilon_{hk} \quad (7)$$

D_{ijhk} is a tensor of the fourth order called stiffness tensor in which 21 independent elastic constants appear.

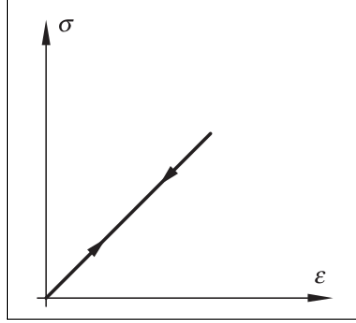


Figure 3: Schematic representation of the stress-strain diagram, linear elastic behaviour , (Lancellotta, 1995).

Introducing the hypothesis of isotropic medium it is possible to arrive at the inverse bond expressed in the form:

$$[\epsilon_{ij}] = -\frac{\nu}{E}\sigma_{kk}\delta_{ij} + \frac{1+\nu}{E}\sigma_{ij} \quad (8)$$

in which the elasticity modulus E and Poisson's ratio ν are shown.

In the case of a specimen subject only to the axial stress component σ_{zz} ($\sigma_{yy}=\sigma_{xx}=0$) by measuring the longitudinal expansion ϵ_{zz} the Young modulus represents the σ_{zz} to ϵ_{zz} ratio, by measuring the lateral contraction suffered by the specimen, the Poisson's ratio corresponds to the ratio between the lateral contraction/dilation and the longitudinal dilation/contraction.

$$E = \frac{\sigma_{zz}}{\epsilon_{zz}} \quad \nu = -\frac{\epsilon_{yy}}{\epsilon_{zz}} = -\frac{\epsilon_{xx}}{\epsilon_{zz}} \quad (9)$$

In an engineering compression test the force applied to the specimen is measured and the initial Section of it is known, from these two quantities it is possible to derive σ_{zz} , Equation (10), from the measurement of the initial and final dimension of the sample it is possible to obtain ϵ_{zz} , ϵ_{yy} , ϵ_{xx} , Equation (11).

$$\sigma_{zz} = \frac{F_{zz}}{A_0} \quad (10)$$

F_{zz} : instantaneously applied load perpendicular to the specimen section, A_0 : initial area of the specimen section.

$$\epsilon_{zz} = \frac{l_{z,i} - l_{z,0}}{l_{z,0}} \quad (11)$$

$l_{z,0}$ is the initial length, $l_{z,i}$ is the instant length. The other longitudinal strains are derived in a similar way.

It is therefore possible to obtain Young's modulus and Poisson's ratio with a simple compression/traction test. The problem with tensile testing and in general in conventional material testing, is that the specimen response is characterized only globally, therefore, in the case of non-homogeneous material or processes, the true material behaviour is lost.

The defects within the material make the macroscopic response to loads different from the homogeneous material behaviour .

To understand how defects modify the material response and correctly identify elastic parameters, it is necessary to have full-field measurements, which provide a field record of a quantity and are well suited to analyze the specific mechanical properties of heterogeneous materials because of their anisotropic and heterogeneous nature.[Viggiani and Hall 2008; Grediac 2004]

For procedures of identification of parameters for constitutive laws it is required the measurement of full field displacements, which can be determined with various techniques, the image correlation is the technique adopted in this work. In particular, digital volume correlation will be performed starting from 3D images of the initial configuration and the deformed configuration of a sample.

3 Tools

In this section the tools that will be used in the work are introduced at a more theoretical level.

3.1 X-ray tomography

X-ray tomography has been firstly commercialized in the 70's for medical applications. It allows to visualize 3D images of the object being scanned.

It is a technique increasingly used in the field of materials science because it provides the possibility to make correlations between the properties of materials and their microstructure. [Salvo et al. 2010; Babout 2006]

The overall concept of X-ray tomography is an extension of classical X-ray radiography, and is based on the attenuation of the X-ray (function of the density) beam through the specimen. X-ray radiography provides only a projection of the sample volume on a single plane, the result is a two-dimensional array. X-ray tomography combines information from a series of projections, each of which is recorded at a different angle between sample and detector. These projections, usually named a scan, are obtained by rotating the specimen, subjected to the x-ray beam.

By assembling the 2D radiographs using a filtered back projection algorithm available in the XAct software (provided by RX-Solutions, Annecy, France), it is possible to obtain the variation of the attenuation of the X-rays in the sample volume. The data is obtained in the form of a three-dimensional array of voxels. The grey value of each voxel describes the X-ray attenuation calculated at that position.

Figure 4a illustrates the principle of X-ray tomograph.

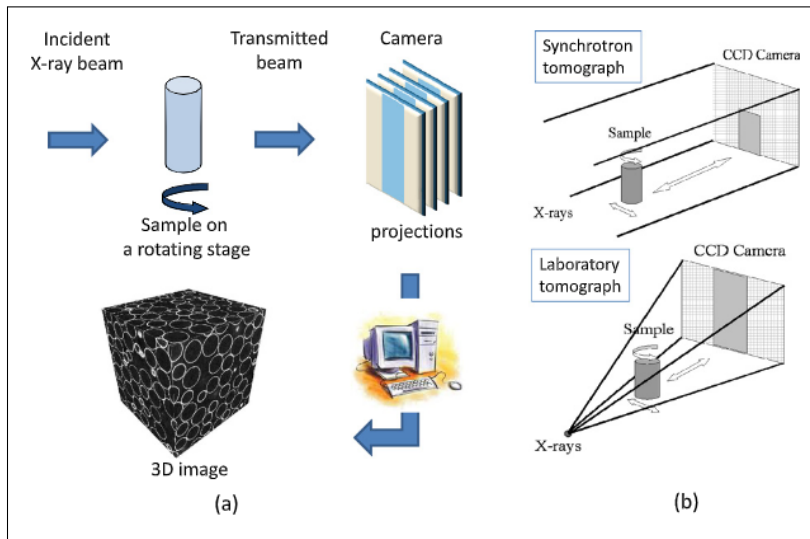


Figure 4: (a) Principle of tomography; (b) Synchrotron and laboratory tomograph. (from [Salvo et al. 2010])

There are two categories of tomographs (Figure 4b): The laboratory tomographs where the X-ray beam is divergent, the spatial resolution varies from a few millimeters down to one micron. The synchrotron sources where the X-ray beam is parallel and the spatial resolution varies between 40 and 0.5 μm .

There are several ways of doing tomography in materials science, in this work laboratory tomography and in particular interrupted in situ tomography has been performed. Interrupted in situ tomography requires specific testing devices (furnaces, compression-tension machine) mounted directly on the tomograph. The same sample is then scanned, mechanical tests need to be interrupted during the scan.

Laboratoire 3SR (Grenoble) hosts a specialised laboratory tomograph built by RX-Solutions (Annecy, France), the setup is shown in Figure 5.

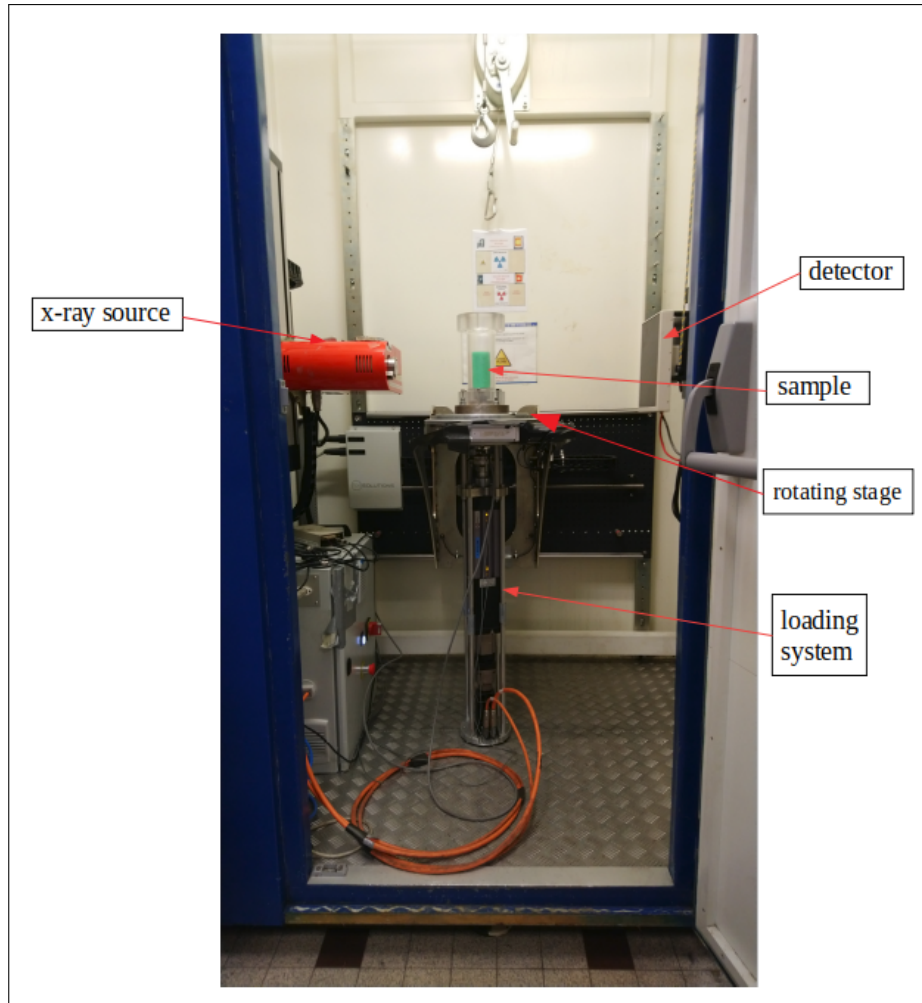


Figure 5: In-situ x-ray facility at Laboratoire 3SR.

The in-situ test starts with a first scan with the unloaded sample, the resulting image is called reference image. After the first scan the loading system is activated, the tests carried out in this case are always uniaxial compression. After the first loading step, this is blocked and a second scan is performed. And so on until the target load is obtained. In this way a 3D image is obtained for each loading step.

As mentioned in the introduction, the one described is one of two methods by which 3D images in initial and deformed configuration are obtained, the synthetic method will be explained later.

3.2 Digital Image Correlation

Digital Image Correlation (DVC), which appeared in the early 1980s ([Lucas et al. 1981]), is designed to measure the displacement fields of surfaces (or in volumes, Digital Volume Correlation) of stressed specimens from images acquired at different stages of loading.[Grédiac and Hild 2012]

The DVC procedure followed in this work is implemented in the open source software spam based on the formulations found in [Lucas et al. 1981], [Hild and Roux 2012] and [Tudisco et al. 2017].

"Spam, the Software for the Practical Analysis of Materials is a Python library that

has evolved to cover needs of data analysis from 3D x-ray tomography work and correlated random fields with mechanical applications." [Stamati et al. 2020]

The input data of the analysis are the gray level distributions, of the image of the first configuration, known as the reference image $f(x)$ and the second configuration, called deformed image $g(x)$. The two images are related to each other from the mechanical transformation Φ_a (called deformation function in spam), following Equation (12)

$$g(\Phi_a(x)) = f(x) \quad (12)$$

The aim is to evaluate the apparent transformation Φ_a on a region of interest (ROI) R of the reference image starting from the knowledge of the gray levels f and g . DVC exploits a texture that must be the signature of each element, simply transported by Φ_a .

Due to acquisition noise and other sources of imperfection [Grédiac and Hild 2012, Hild and Roux 2012], Equation (12) is actually never strictly satisfied. Therefore, it is normally formalised to tolerate white Gaussian noise and is written in a weak form over the domain of interest (containing more than 1 voxel).

The correlation procedure here consists in minimising the sum of squared differences (SSD) between the reference image, $f(x)$, and the deformed one, $g(x)$, corrected by $\Phi_0(x)$ (Equation 13). Note that this similarity criterion is compatible with the assumption of white Gaussian noise [Buljac et al. 2018].

This problem is solved through an iterative procedure (spam used the Newton-Raphson method), until convergence is achieved.

$$C = \int_R [f(x) - g(\Phi_0(x))]^2 dx \quad (13)$$

This quantity is null when $\Phi_0(x)$ is equal to $\Phi_a(x)$. However, in real cases C can't not be zero, due to acquisition noise and other sources of imperfection.

In this work the local approach will be exploited in which the transformation Φ_0 over R is decomposed into a multitude of independent and local transformations calculated in independent subvolumes called zones of interest (ZOIs) or correlation window, the outcome is a field of discrete deformation functions for the whole region of interest. [Stamati 2020]

The size of the correlation window is strongly related to the texture of the material.

In SPAM the convergence criterion which is implemented is based on the norm of the deformation function increment between two successive iteration steps, it is set to $\|\delta\Phi\| < 10^{-6}$.

In order for Newton-Raphson's method to converge it is necessary to insert a first guess that is close enough to the right solution. This first step is obtained considering the whole images as the domain for correlation. What is obtained is a single deformation function called registration Φ_{reg} .

As already mentioned, for the iterative algorithm to converge, each local calculation should start close enough to the right solution. Therefore, the application of the computed registration Φ_{reg} to each point of the grid is most of the times an essential initial guess.

The code for the Local Digital Image Correlation will return, for each measurement point/node (thus the centre of correlation window), a specific Φ_0 , along with the following information:

- The point's number;
- The point's Z,Y,X position;
- The point's Z,Y,X displacement;
- The error for each sub-volume: final difference in grey-levels between the reference image and $g(\Phi_0(x))$ subvolumes with a normalisation applied;
- The number of iterations until convergence (equal to the number of maximum iterations if convergence is not reached);

- The return status:
 - 2 = Convergence: reached desired $\delta\Phi_{min}$;
 - 1 = Not Convergence: stopped by hitting the maximum number of iterations without diverging;
 - -1 = Divergence: error is more than 80% of previous iteration error;
 - -2 = Iterative procedure stopped: singular matrix M cannot be inverted;
 - -3 = Divergence: diverged on displacement or volumetric change condition;
 - -4 = Margin alignment for reference image and deformed image subvolumes failed (the iterative procedure never started);
 - -5 = Greylevel condition or mask failed (the iterative procedure never started);
 - -6 = NaNs in initial Φ field (probably coming from pixel search or input binned field);

For more information [SPAM, documentation].

3.3 Finite Element simulation

As will be explained later, the step after the LDIC, for procedures of identification, are finite element simulations. This requires the generation of a FE mesh which represents the initial configuration of the material.

SPAM is used to create the mesh (unstructured 3D mesh made of 4-node tetrahedra) and to project morphology into it. From the 3D image of the initial configuration it is possible to extract the characteristics of the morphology of the meso-structure.

The first thing to do is to identify the different phases in the image, assigning to each one a precise value.

In case the image comes from x-ray tomography, the gray values represent the attenuation coefficient inside the scanned sample, so dense phases are characterized by high grayvalues, low-density phases by low grayvalues.

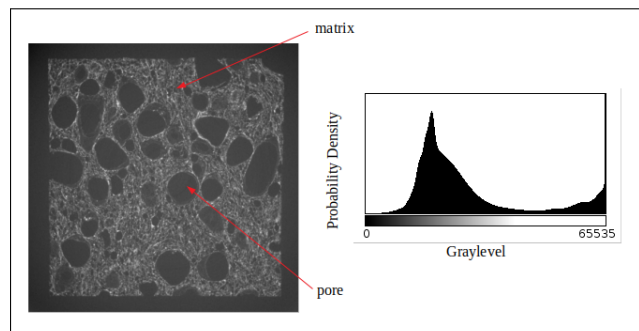


Figure 6: Representative vertical slices and greylevel histograms of the corresponding reconstructed 3D volumes for a uniaxial tension.

Figure 6 shows the vertical central slice of the reconstructed 3D images coming from the first (before loading) scans of a uniaxial tension. By eye the different phases are easily distinguishable.

If the phases have very different densities, the gray values will have an easily identifiable threshold, directly obtaining a binary image in which 0 represents phase(1) and 1 represents phase(2).

However, in the case shown in Figure 6, the matrix has low density, which leads to grayvalues similar to those in correspondence of the voids.

At the scale of observation, however, the matrix is a more heterogeneous material compared to pore. This means that the variation of greyvalues inside this material should be more irregular. Instead of separating the solid phase based on the absolute greyvalues, is adopted an approach

that is based on the variation of the greyvalues.

The variance map of the 3D image is calculated. It is based on a selected structuring element, given by the formula: $VAR(X) = E(X^2) - E(X)^2$, where $E(X)$ is the averaged greyscale image over a structuring element (binary matrix, defined by its shape and size, that selects a local neighbourhood around a voxel of interest). The structuring element should be just large enough to separate low and high variance regions, while remaining sufficiently small to capture the smallest pore to be segmented, but also to preserve the details of the pore's shapes.

The computed variance map of the representative vertical slice (cropped) is shown in Figure 7a. Afterwards, by isolating with a thresholding operation the lower variance areas (pores) and discarding the, a binary image containing only the segmented matrix is obtained (see Figure 7b).

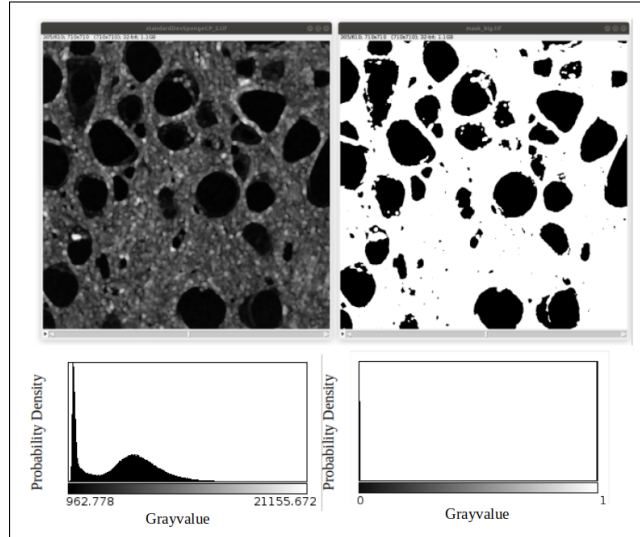


Figure 7: Representative vertical slices and greylevel histograms of the corresponding reconstructed 3D volumes for a uniaxial tension.

Once the binary image is obtained, it is possible to continue with the creation of a “homogeneous” FE mesh, independently of any morphology, as can be seen in Figure 8a.

the first operation consists in projecting the identified morphology onto the FE mesh. The first step in order to project the phases onto a mesh is to compute a distance field corresponding to each inclusion type phase.

Using this field instead of a raw binary phase field is mandatory since the computation of the interface vector requires a gradient to compute a accurate orientation.

In the reported case there is only one phase beyond the matrix, so it is necessary to make only one distance field.

Finally the final FE mesh is created by projecting the distance field file (pores) into the empty FE mesh. In Figure 8b, the final result can be seen.

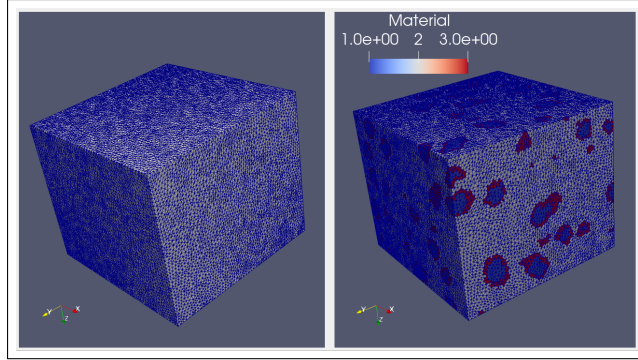


Figure 8: Unstructured 3D mesh made of 4-node tetrahedra, and FE mesh which represents the initial configuration of the material.

Once the mesh is generated the simulations are performed by FEAP (Finite Element Analysis Program). [Taylor 2014].

In FEAP the required inputs, in addition to the mesh itself, are the constitutive law (linear elastic) and the type of loading.

The purpose of the simulations is to realistically recreate the test that generated the deformed configuration $g(x)$.

There are various kinds of loading that can be used including fixed displacement [Maire and Withers 2014, Rieger et al. 2018], fixed stress [Veyhl et al. 2011], or using an effective medium surrounding the sample [Maire et al. 2007].

In this work to deform the specimen, instead of using idealised boundary conditions, are used the boundary conditions extracted from the displacement field obtained by the LDIC.

In every simulation it is necessary to insert also the elastic parameters. These are not known and the final output of the procedure. The Equilibrium Gap Method is used to identify them.

3.4 Equilibrium Gap Method, EGM

In order to do the identification, over the years, different methods based on the kinematics measurements and FE simulation have been developed, such as the "Constitutive Equation Gap Method" [Ladeveze and Leguillon 1983], the "Reciprocity Gap Method" [Bui 1995], the "Equilibrium Gap Method" [Claire et al. 2004] or the "Finite Element Updating" [Kavanagh and Clough 1971].

In this study is followed the Equilibrium Gap Method. It involves considering a wide range of different elastic parameters that are simulated. A *simulated* displacement field is derived from each simulation. Minimizing the difference between the *real* displacement field produced by DVC and the *simulated* displacement fields obtained with FE (called displacement residual) allows to obtain the simulation more similar to reality, the one in which the input parameters are, approximately, the elastic parameters of the material.[Grédiac and Hild 2012]

4 Simulated kinematic fields

The first procedure that is studied is the one without experimental campaign, in which therefore the displacement field does not come from a real test, but from a simulated test.

The Figure 9 where the whole procedure is schematically shown, is explained in the next section. (4.1).

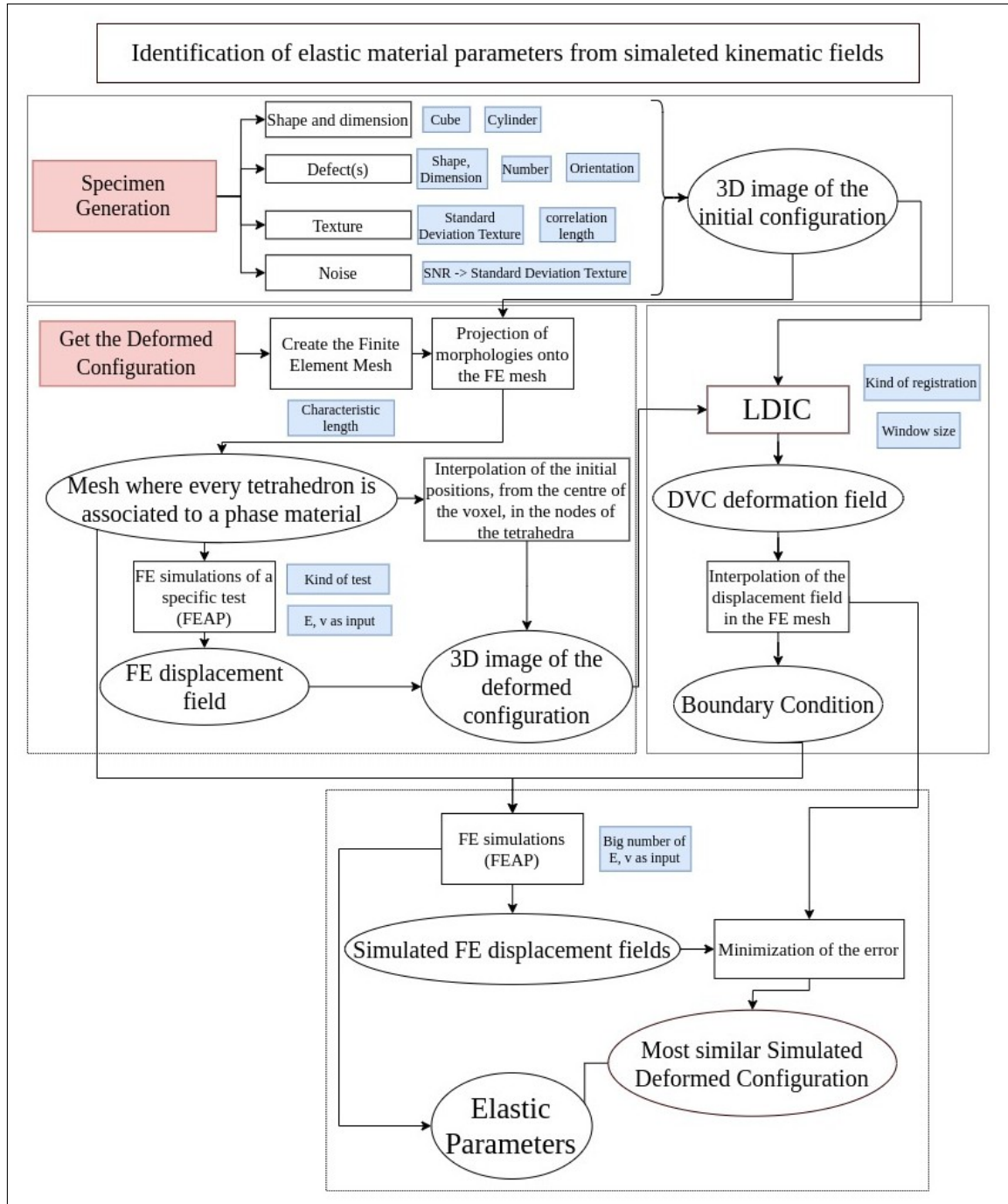


Figure 9: Project flowchart for identification of elastic material parameters from simulated kinematic fields.

4.1 Methodology, Homogeneous case

This Section explains the methodology needed to complete the procedure with a purely simulated approach, going to exploit the first application: **homogeneous case**.

In Figure 9 the work is schematized, the flowchart is divided into 4 sections, below, each of these steps is explained.

The homogeneous case is the first one that is treated because it is useful to define the order of magnitude of the error between the actual displacement field and the simulated displacement field in the basic case (using exactly the input elastic parameters).

This analysis is divided into two parts: homogeneous material, no noise and homogeneous material, presence of noise.

The procedure is useful to identify the effect that parameters have on the displacement field. Once the parametric analysis has been completed, the identification of the Poisson's ratio is carried out.

4.1.1 Step 1: Specimen Generation

In Figure 10 the first step is extracted from the general flowchart.

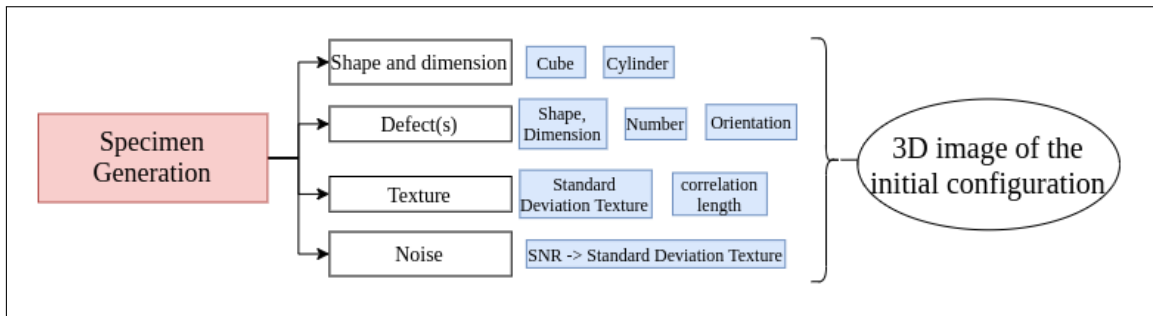


Figure 10: Project flowchart for Specimen generation.

In the absence of experimental outputs, it is necessary to generate an image of the initial configuration.

In this first operation the parameters whose effects are interesting are many, first of all the shape and size of the sample itself. To understand the effects of these also in relation to the calculation time.

A cube with a 141 mm (Figure 11) side is chosen to begin with. This measurement will then be increased finding the Poisson's ratio more precisely without affecting the times too much.

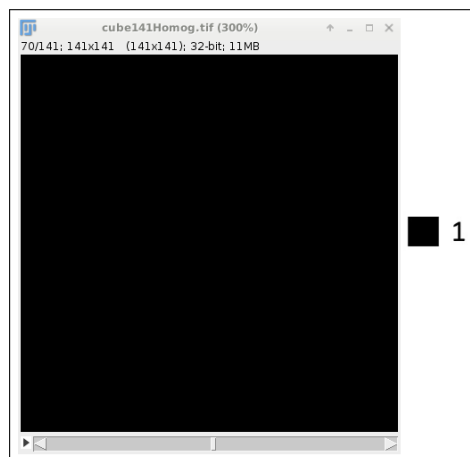


Figure 11: cube, $l = 141$ mm, central cut, No Texture.

Once the basic specimen has been generated, it is possible to insert the defects inside it, thus

generating different types of configuration modifying the shape, size, position, number, orientation and mechanical properties of the defects in relation to the matrix. For the homogeneous case this operation is not done.

At this point it is necessary, for the purpose of image correlation, to add a texture to the specimen. To do this, a random field based on a normal distribution is added to the gray values of the image, using Spam. The random field is characterized by the standard deviation, how each value moves away from the mean value, and by a correlation length. The correlation length is the characteristic distance over which the normalised pair correlation function of the signal decays to 50%, the smaller the correlation length the finer the texture and vice versa. When the correlation length is too small, i.e., in the order of one pixel, the signal might no longer be distinguished from the noise. When is too big, close to the size of the DVC correlation window, there will not be a good texture to exploit and the correlation presents difficulties.

The following correlation lengths are used for the parametric analysis:

- No noise: correlation length = 3, 5, 10 mm;
- With noise: correlation length = 3, 7 mm.

The random field in Figure 12 has a **standard deviation of 0.3** and a **correlation length (lc) of 3, 5 and 10 mm**.

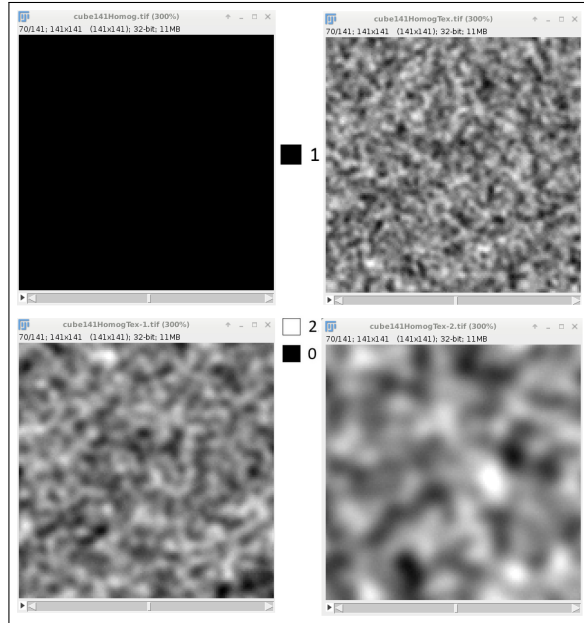


Figure 12: cube, l = 141 mm, central cut, No Texture, lc = 3-5-10 mm

Finally, it is important to remember that each measurement is error-prone, so to make the synthetic images more realistic, normally distributed Gaussian noise is added to each voxel. The standard deviation of the Gaussian noise is selected based on the resulted Signal to Noise Ratio (SNR), which is defined as:

$$SNR = \frac{\sigma_{TX} + \sigma_{noise}}{\sigma_{noise}} \rightarrow \sigma_{noise} = \frac{\sigma_{TX}}{SNR} \quad (14)$$

In general:

- SNR = 10 acceptable image quality;
- SNR = 40 excellent image quality.

The following SNR are used for the parametric analysis:

- With noise: SNR = 10, 20, 30, 40.

In Figure 13 the Gaussian noise with a SNR = 10 (a) and SNR = 40 (b) is added to a configuration with correlation length = 3 mm.

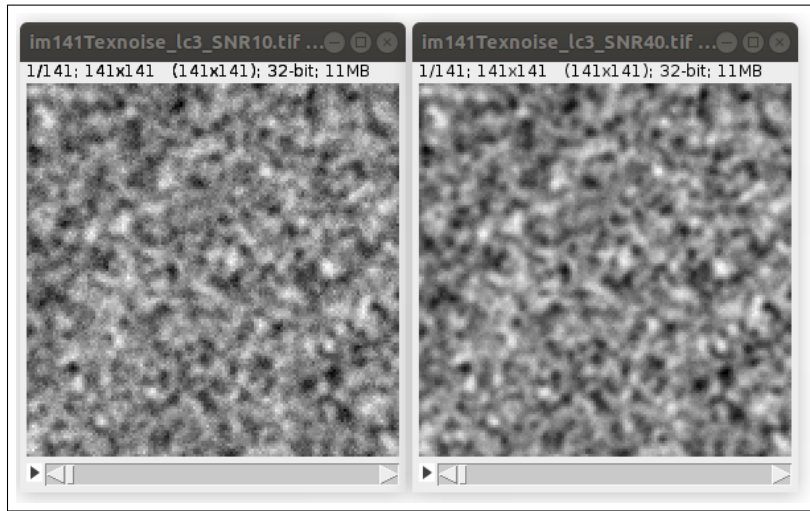


Figure 13: cube, $l = 141$ mm, central cut, $lc = 3$ mm, SNR = 10 and SNR = 40

4.1.2 Step 2: Deformed configuration

Generated the initial specimen with a texture suitable for correlation, and realistic noise, it is necessary to generate the deformed configuration of the specimen itself. In Figure 14 the procedure to obtain the deformed configuration is schematised.

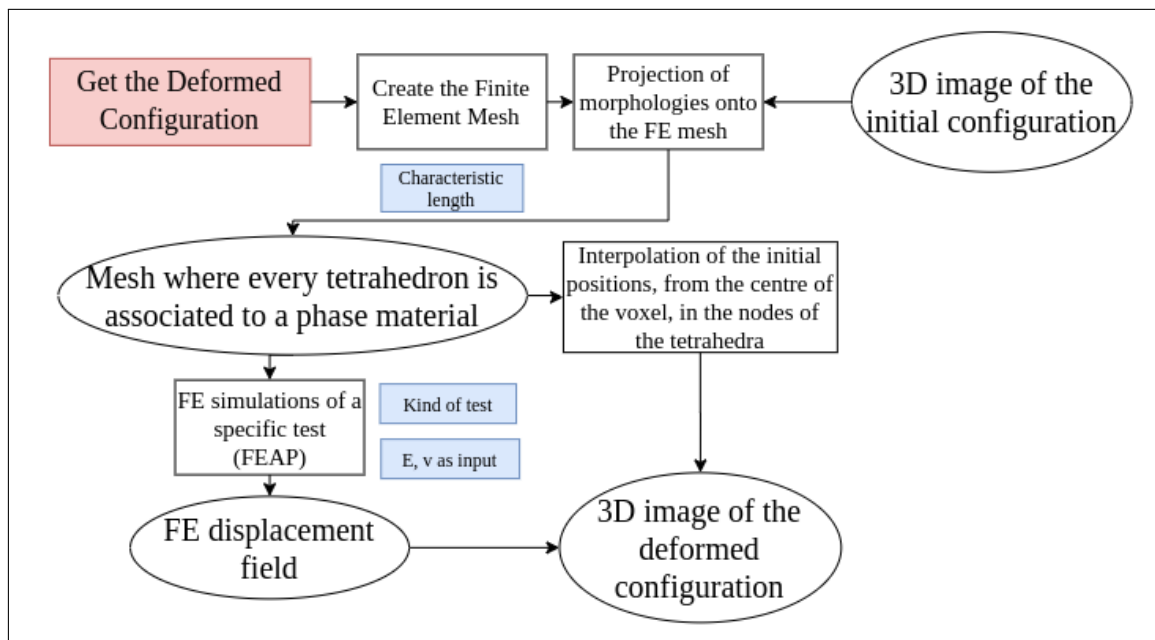


Figure 14: Project flowchart for Deformed configuration generation.

This step can be divided into:

- FE Mesh Generation
- Deformed configuration (as a mesh)
- Deformed configuration (as an image)

In order to obtain the deformed configuration, finite element simulations are performed, using the FEAP software. In this case the parameters to work with are first the parameter of the mesh, which is a FE mesh of 4-noded tetrahedra elements, generated with randomly and evenly distributed nodes in space, the parameter, that can be specified, is the characteristic spacing between nodes (l_{char}).

Second, the parameters of the simulation:

- Type of loading that is applied to the specimen;
- Elastic parameters (these are the input parameters, those that should be found at the end of the discussion).

Being the homogeneous case the generic 141 mm side mesh is already the mesh where every tetrahedron is associated to a phase of the material, so the step that involves the projection of the morphology can be skipped, as reference see Figure 8 from Section 3.3.

In general it is necessary to project the initial configuration, in the generic mesh with the dimensions in mm of the sample (note in general the images have dimensions in px).

Four different meshes are simulated, with different **characteristic spacing between FE nodes, $l_{char} = 3, 5, 7, 10$** , shown in Figure 15.

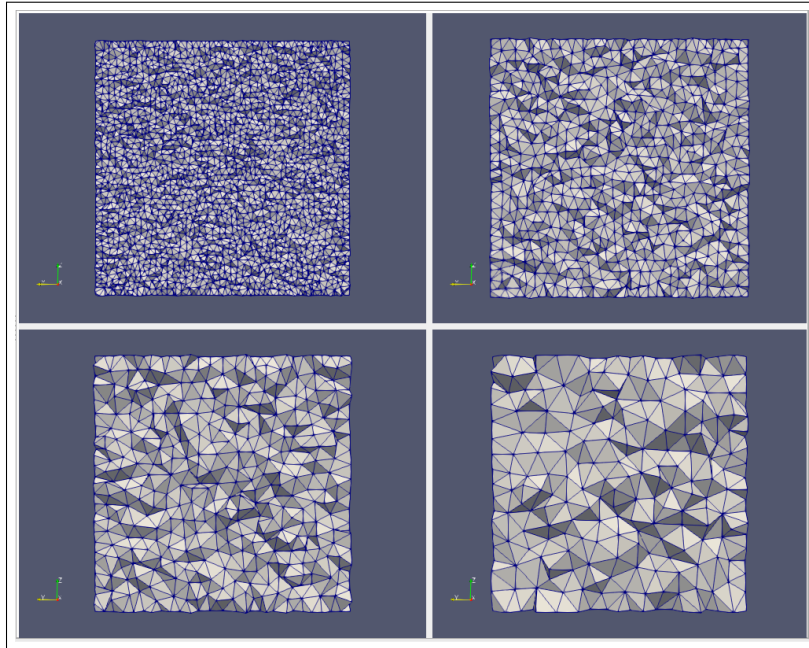


Figure 15: cube, $l = 141$ mm, central cut, $l_{char} = 3$ mm, $l_{char} = 5$ mm, $l_{char} = 7$ mm, $l_{char} = 10$ mm.

Once the mesh is created it is possible to proceed with the simulation, obtaining as output the deformed configuration (displacement field) as seen in Figure 16.

In the simulation is applied a **displacement of 3 mm in the Z direction** to the top of the sample and fixed base. The **elastic parameters** chosen are:

- $E = 10e3$ (MPa);
- $\nu = 0.2$.

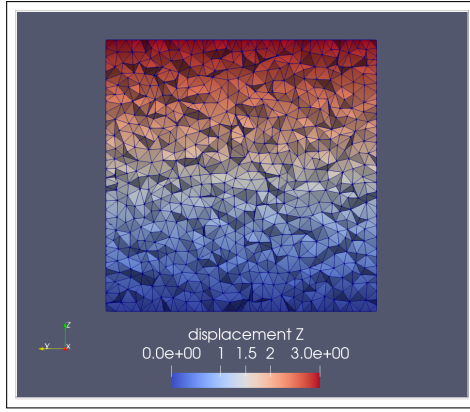


Figure 16: Axial displacement field in a FE mesh with $lchar = 5$ mm, applied displacement: 3 mm in z direction in $z = 141$ mm.

From the FE simulation the displacements in the nodes of each tetrahedron are obtained. To get an image of the deformed configuration it is necessary to interpolate the information, present in correspondence of the nodes, in the centres of each voxel of the image of the initial configuration. In this way from the FE simulation the images of synthetic deformed configurations are obtained, as shown Figure 17.

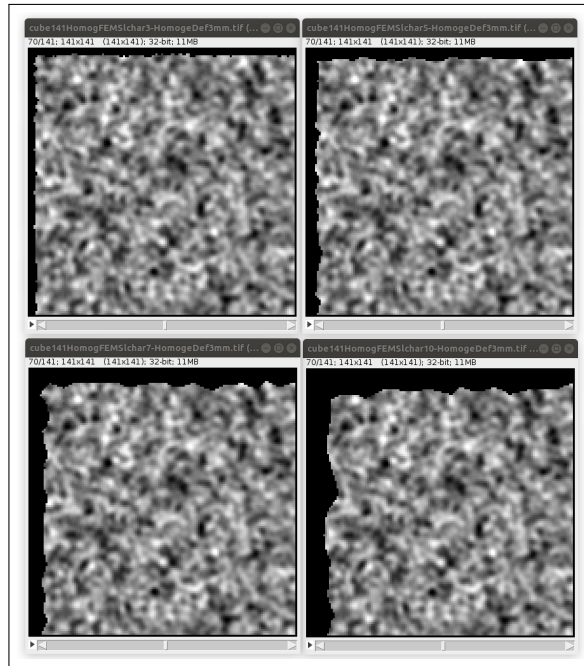


Figure 17: Deformed configuration as image, $lchar = 3-5-7-10$ mm, applied displacement: 3 mm in z direction in $z = 141$ mm

If the analysis is done considering also the noise at this point a random distribution similar (with the same parameters) to the one added to the initial configuration must be added, to the simulated deformed image. As per the final step of the specimen generation described in Section 4.1.1.

4.1.3 Step 3: Local Digital Volume Correlation, Extracting the boundary conditions

In Figure 18 the third step is extracted from the general flowchart.

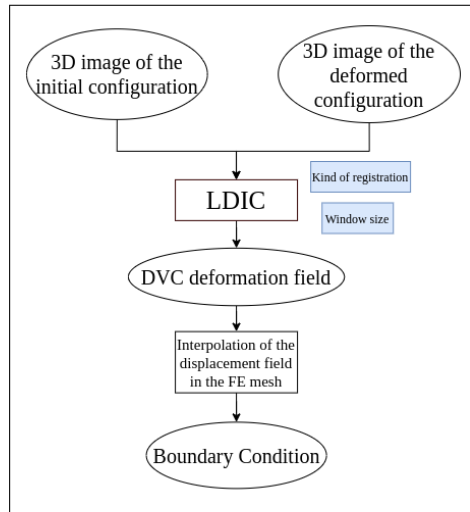


Figure 18: Project flowchart for Extracting the boundary conditions.

This step can be divided into:

- Getting L-DIC displacement field
- Interpolation of the DVC displacement field to the nodes of the FE mesh
- Extracting the boundary conditions

Once the two images corresponding to the initial and final configuration have been obtained, the next step is to use the LDIC in order to measure the displacement field that maps the reference to the deformed image. An important parameter for LDIC is the correlation window which is related to texture of the matrix material and size of the defects. For each configuration of the parametric analysis (different l_c , l_{char} and SNR) an L-DIC with **half windows size, hws, of 3, 7 and 14 mm** is made.

The displacement field in spam gives information about translation, rotation and normal and shear strain in each correlation window. In order to obtain the correlation of most of the points it is necessary to help the L-DIC with an initial guess. This initial guess is obtained by comparing the two overall images getting the deformation in the centre of the image. Below are shown in Figure 19 and Figure 20, the return status (see chapter 3.2) and the displacements in z direction, for the case Correlation length = 3 mm, Characteristic length = 3 mm.

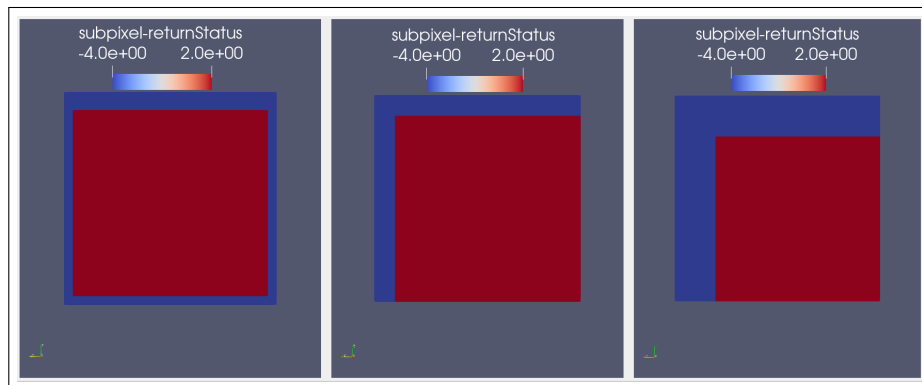


Figure 19: Results from LDIC, return status, $l_c = 3$ mm, $l_{char} = 3$ mm, $hws = 3, 7$ and 14 .

For each correlation window are given information about the status of the procedure, can be seen how for most of the windows $RS = 2$, which as mentioned in the chapter 3.2 means that in those windows the correlation is successful.

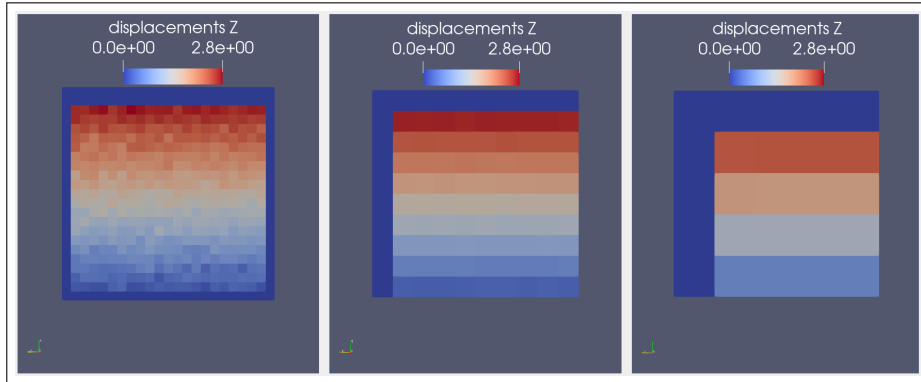


Figure 20: Results from LDIC, $lc = 3$ mm, $lchar = 3$ mm, axial displacement field, $hws = 3, 7$ and 14 mm.

Figure 20 shows how the smaller the correlation window size, the more measurement points, which results in a highly spatially resolved displacement field, however, having less information to correlate, the noise is higher. With bigger window, local information might be lost, but the displacement field is less noisy.

The next step is the interpolation of the DVC displacement field to the nodes of the FE mesh. As can be seen from the previous pictures, the outermost frame of points do not correlate, so it is advisable to delete these points. At this point the interpolation of the data from the centre of the voxels to the tetrahedra nodes of the mesh of the cropped image is done as seen in Figure 21.

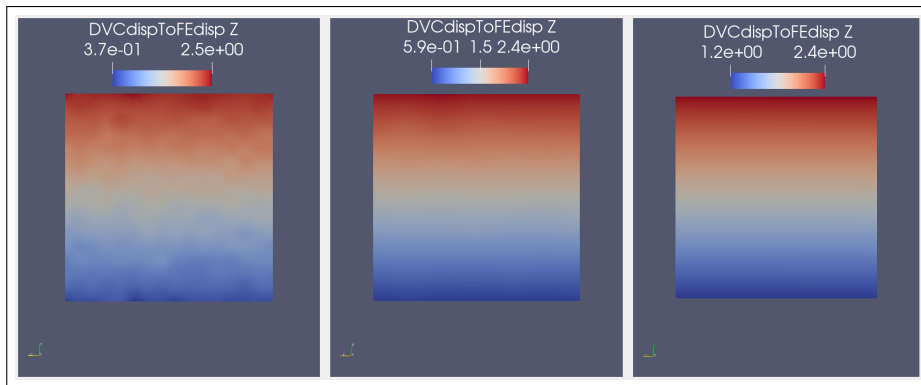


Figure 21: Axial displacement field from DVC interpolated using the mesh, $lc = 3$ mm, $lchar = 3$ mm, $hws = 3, 7$ and 14 .

From the Figure 21 it is possible to notice how, for small correlation windows, the displacement field is more noisy.

Finally it is possible to extract the boundary conditions as seen in Figure 22.

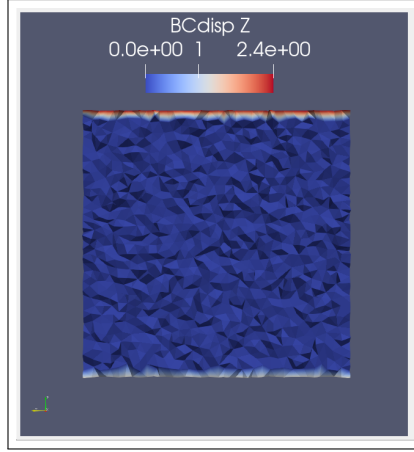


Figure 22: Boundary Condition, $l_c = 3$ mm, $l_{char} = 3$ mm, $h_{ws} = 7$ mm.

4.1.4 Inter Step: reference residual field

The reference residual field is the displacement residual between the real deformed configuration and the simulated deformed configuration, using in the simulation the same input elastic parameters.

This analysis is divided into two parts:

- Homogeneous material, no noise;
- Homogeneous material, presence of noise.

The procedure is useful to identify the effect that the previously discussed parameters have on the displacement field.

Once the reference values for the residuals have been obtained, the identification of the Poisson's ratio is carried out.

In order to obtain the simulated deformed configuration in Figure 23, a FE simulation is performed by **applying the boundary conditions**, visible in Figure 22. The elastic parameters chosen are the same as the "real" deformed configuration:

- $E = 10e3$ (MPa);
- $\nu = 0.2$.

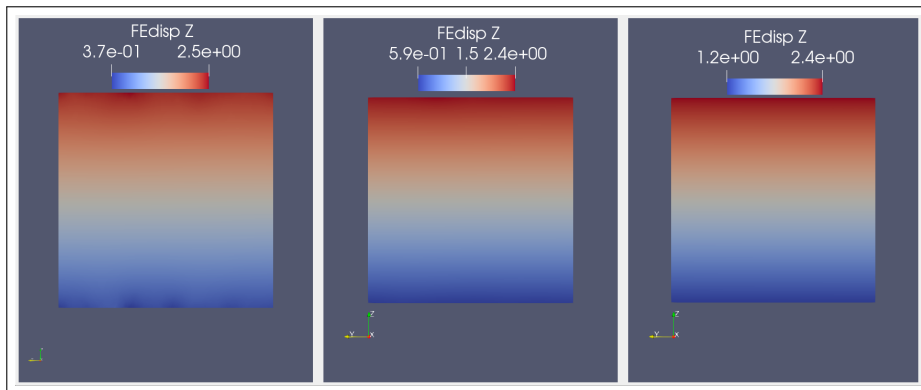


Figure 23: Simulated displacement field, $l_c = 3$ mm, $l_{char} = 3$ mm, $h_{ws} = 3, 7$ and 14 mm.

By subtracting the interpolated displacement field (Figure 21) and the simulated displacement field (Figure 23) the residuals are obtained, each for each configuration.

$$residual_i = \|u_i^{DVCToFE} - u_i^{Simulated}\| \quad (15)$$

- u: displacement;
- i: displacement component.

In order for the residual to be more significant, it is good to normalize it, using maximum displacement.

$$residual_{i, Norm} = \frac{\|u_i^{DVCtoFe} - u_i^{Simulated}\|}{u_{i, max}^{DVCtoFe}} \quad (16)$$

No Noise

Below are the middle sections of six of the fields obtained in the analysis without noise.

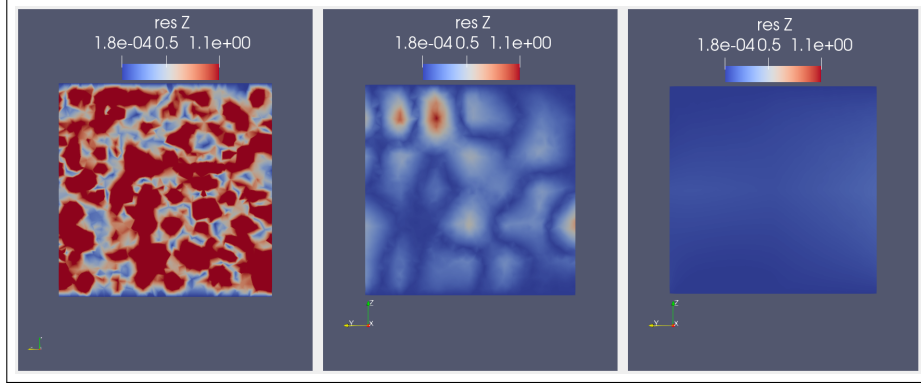


Figure 24: Displacement residual, direction z, cube, $l = 141$ mm, central cut, $lc = 3$ mm, $lchar = 3$ mm, $hws = 3, 7$ and 14 mm.

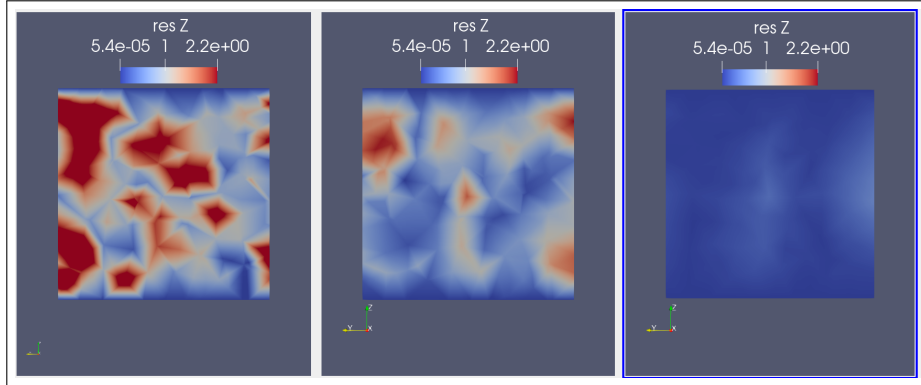


Figure 25: Displacement residual, direction z, cube $l = 141$ mm, central cut, $lc = 10$ mm, $lchar = 10$ mm, $hws = 3, 7$ and 14 mm.

In order to quantify not only visually, but also mathematically which set of parameters leads to the simulated deformed configuration closer to the reference one, the following error definition between the two displacement fields is used:

$$error_i = \frac{1}{N} \sum_{n=0}^{n=N} \frac{\|u_i^{DVCtoFe} - u_i^{Simulated}\|}{\|u_i^{DVCtoFe}\|} \quad (17)$$

- i: displacement and error component;
- n: each nodes of the mesh;
- N: total number of nodes of the mesh.

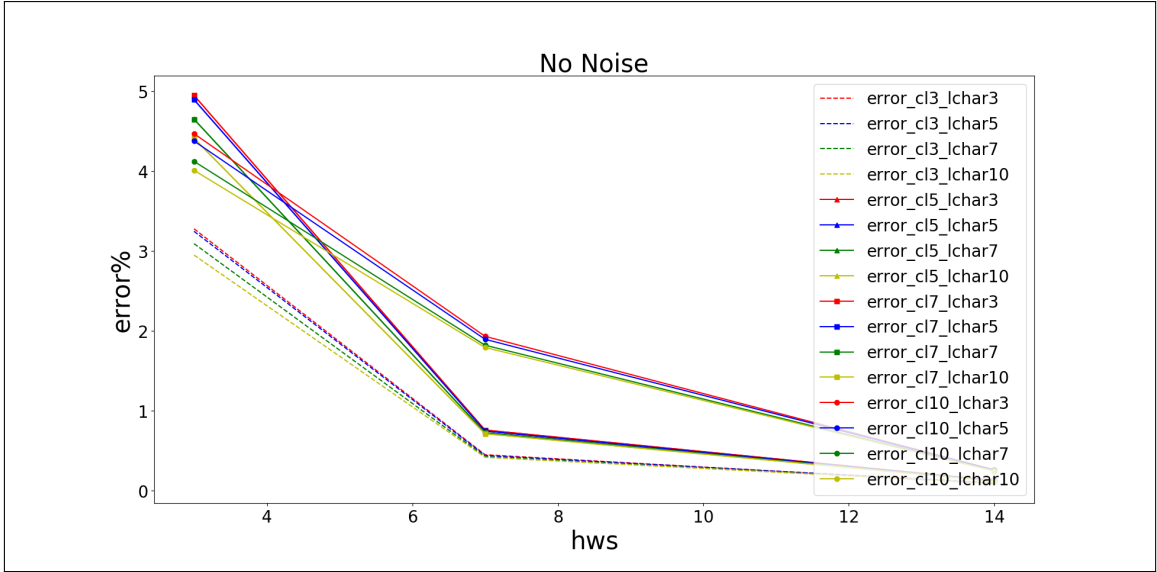


Figure 26: Error, cube, $l = 141$ mm, No Noise, $lc = 3, 5$ and 10 mm, $lchar = 3, 5, 7$ and 10 mm, $hws = 3, 7$ and 14 mm.

In order to have a clearer idea of the trends, errors are reported for each case in Figure 26.

Comparing these values can be seen that in the homogeneous case the finer the texture (lc smaller) the smaller the error, the curves are joined in groups of four meaning that the characteristic length of the mesh does not influence the results (as it is logical to expect for an homogeneous case). The most influential parameter is the correlation window the higher it is, the better the results. Once the hws is 14 the other parameters lose relevance.

With Noise

At first realistic noise levels are used, following the definition of Signal to Noise Ratio seen above. The parameters used are:

- $lc = 3, 7$;
- $SNR = 10$ (acceptable), $20, 30, 40$ (excellent);
- $lchar = 3, 7$;
- $hws = 3, 7, 14$.

One of the objectives of parametric analysis with noise is to find a value of SNR such as to have a jump in error. The noise levels analysed made the errors increase but the results are always acceptable (except for $hws = 3$), as can be seen in Figure 27a, so in a second phase, the error levels have been increased, decreasing the **SNR: 2, 4, 6, 8**, just for the case $lc3, lchar3, hws3-7-14$.

Observing the errors that are obtained in Figure 27b it is possible to notice the jump between acceptable and not acceptable for $SNR 4$ and a big jump for $SNR 2$.

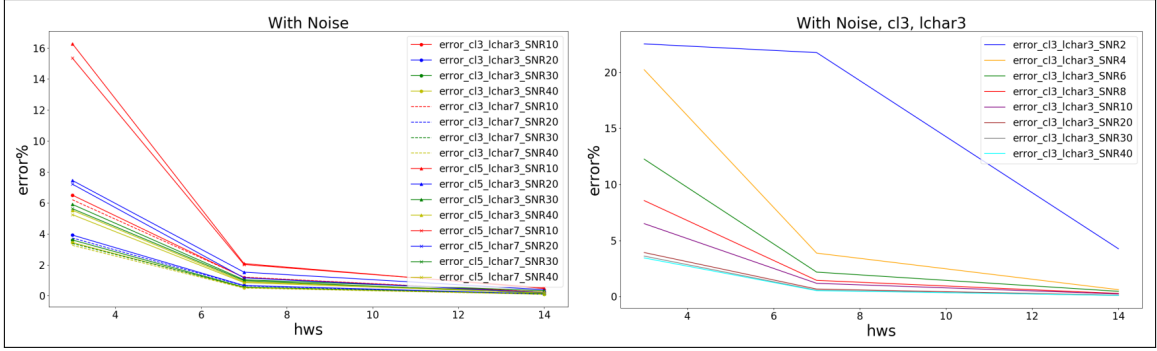


Figure 27: Error, cube, $l = 141$ mm, With Noise, $lc = 3, 5$ mm, $lchar = 3, 7$ mm, $hws = 3, 7$ and 14 mm, $SNR = 10, 20, 30, 40$ (a). Error, cube, $l = 141$ mm, With Noise, $lc = 3$ mm, $lchar = 3$ mm, $hws = 3, 7$ and 14 mm, $SNR = 2, 4, 6, 8, 10, 20, 30, 40$ (b).

If for $hws = 7$ and 14 even with a noise level equal to $SNR = 4$ an acceptable error is obtained in the case of $hws = 3$ a good result is achieved for $SNR = 10$.

4.1.5 Step 4: Identification of elastic parameters

In Figure 28 the fourth step is extracted from the general flowchart.

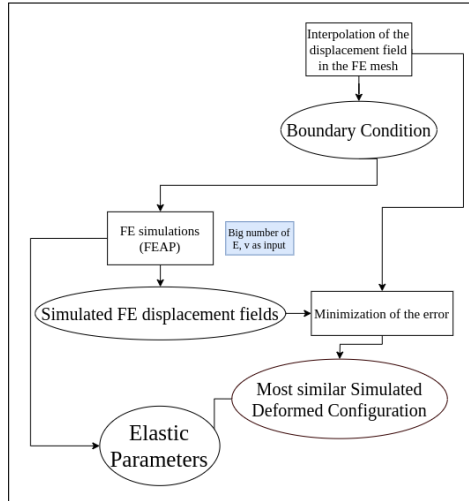


Figure 28: Project flowchart for the identification.

This step can be divided into:

- Simulated deformed configurations
- Identification of elastic parameters

In order to obtain the simulated deformed configurations, a number FE simulations are performed by applying the boundary conditions, shown in Figure 22 and different elastic parameters in each configuration. In order to identify the elastic parameters, the error, defined in Equation (17), obtained by comparing the interpolated displacements from the DVC and the simulated displacement fields is minimized. In practice what is done is to compute the error for each input Poisson's ratio. These error values are then used to approximate an interpolation function (cubic), the minimisation (Nelder–Mead method) of which leads to the identification of the Poisson's ratio.

Having analysed the effects that the various parameters have with respect to the generation of errors in the displacements, it is possible to begin to evaluate, for a single case, the errors in the evaluation of the elastic parameters.

For the homogeneous case Young's modulus does not influence the displacements, as the stress are not known. Therefore the identification focuses only on Poisson's ratio. It is possible to identify the ratio of the Young's moduli when two materials (matrix, particles) are present.

The case under analysis is the following:

- cube side 141 mm (cropping to a cube side 100 mm);
- $l_c = 3$ mm, $l_{char} = 3$ mm, $h_{ws} = 7$;
- No noise, SNR = 2, 4, 6, 10, 20;
- Applied deformation 3 mm in the z direction to the top of the sample and fixed base, input parameters: $\nu = 0.2$, $E = 10e3$ MPa;
- Different simulated deformed configurations with different Poisson's ratios as input:

$$\nu_{simulated} = [0.15, 0.25, 0.01] \quad (18)$$

Obtained all displacement fields, the error is evaluated:

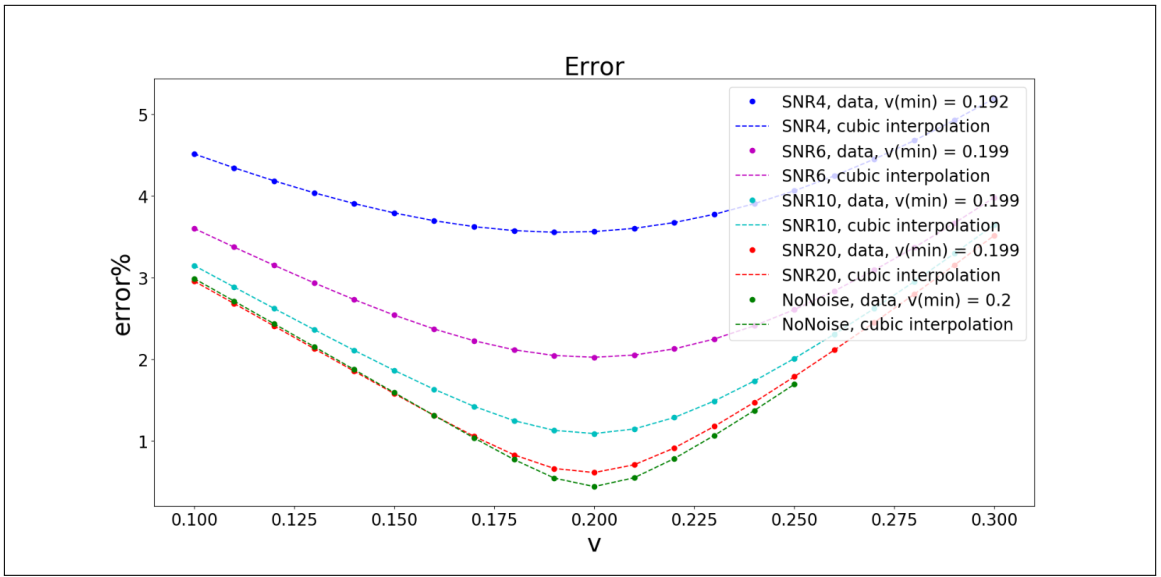


Figure 29: Identification homogeneous material, traction.

The results for the identification of the homogeneous case subjected to traction can be seen in Table 1.

Identification ν	$l = 141$ mm, $l_c = 3$ mm, $l_{char} = 3$ mm, $h_{ws} = 7$
input	$\nu = 0.20$
No Noise	$\nu_{min} = 0.200$
SNR = 20	$\nu_{min} = 0.200$
SNR = 10	$\nu_{min} = 0.199$
SNR = 6	$\nu_{min} = 0.199$
SNR = 4	$\nu_{min} = 0.192$
SNR = 2	$\nu_{min} = -$

Table 1: Identification homogeneous material, traction.

By varying the noise good results are obtain up to SNR = 6, for SNR = 4 the procedure can find a ν value, but it is far from the input value, for SNR = 2 no result can be found.

Once the identification for this simple homogeneous case is verified, it is useful to confirm that for different types of load and sample size the minimum of the error function is in the immediate vicinity of the input Poisson's ratio value.

A comparison is made between:

- Cube 141, $l_c = 3$ mm, $l_{char} = 3$ mm, $h_{ws} = 7$, input parameters: $\nu = 0.2$, $E = 10e3$ MPa, imposed deformation = +3 mm z direction (**traction**), No noise, SNR = 2, 4, 6, 10, 20;
- Cube 141, $l_c = 3$ mm, $l_{char} = 3$ mm, $h_{ws} = 7$, input parameters: $\nu = 0.2$, $E = 10e3$ MPa, imposed deformation = -3 mm z direction (**compression**), No noise, SNR = 2, 4, 6, 10, 20;
- Cube 141, $l_c = 3$ mm, $l_{char} = 3$ mm, $h_{ws} = 7$, input parameters: $\nu = 0.2$, $E = 10e3$ MPa, imposed deformation = +3 mm x direction ("**shear**"), No noise, SNR = 2, 4, 6, 10, 20;
- Cube 400, $l_c = 3$ mm, $l_{char} = 3$ mm, $h_{ws} = 7$, input parameters: $\nu = 0.2$, $E = 10e3$ MPa, imposed deformation = +8.51 mm z direction (**traction**), No noise, SNR = 2, 4, 6, 10, 20;

For the large specimen an imposed deformation = +8.51 mm z direction is chosen, so that it is in proportion to the deformation applied to the small specimen.

These four configurations can be seen in Figures 30.

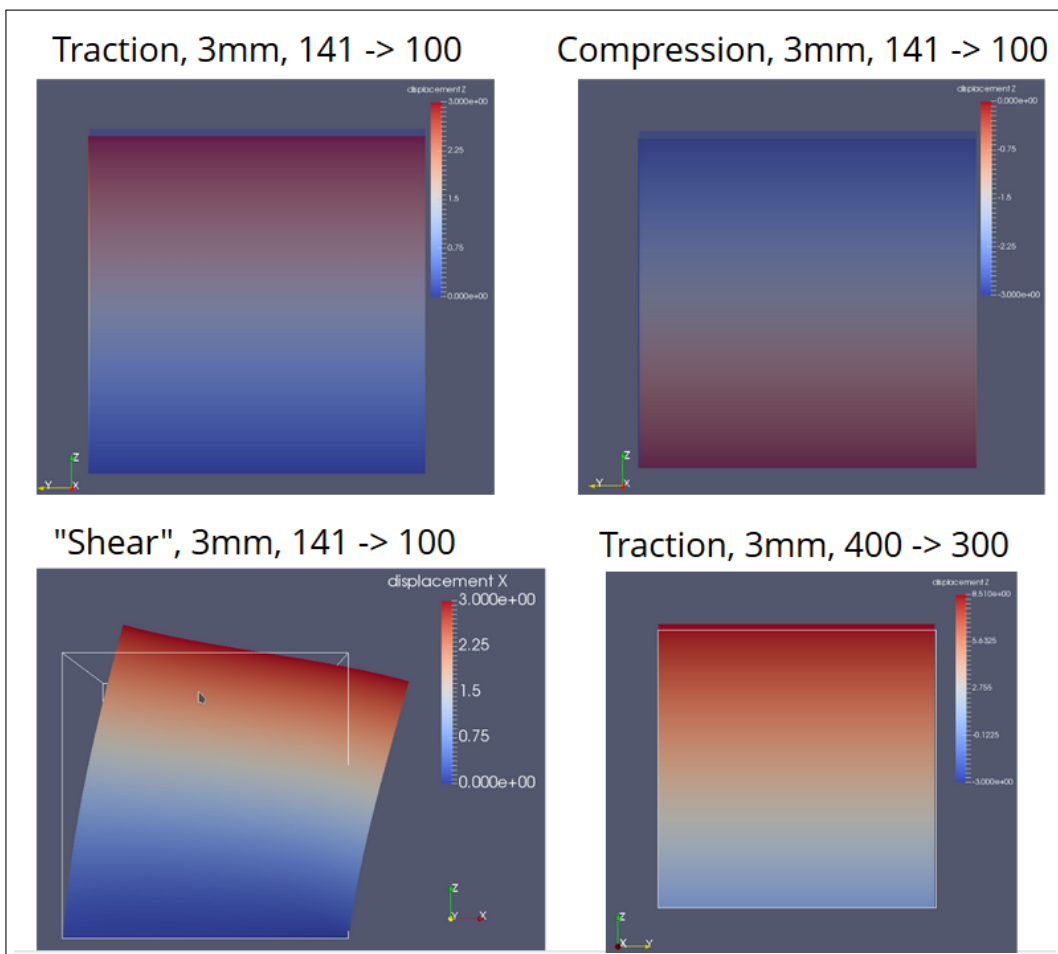


Figure 30: Homogeneous cases, different types of load and sample size.

The results of the identification are visible in Figure 31 and more summarized in the table 2.

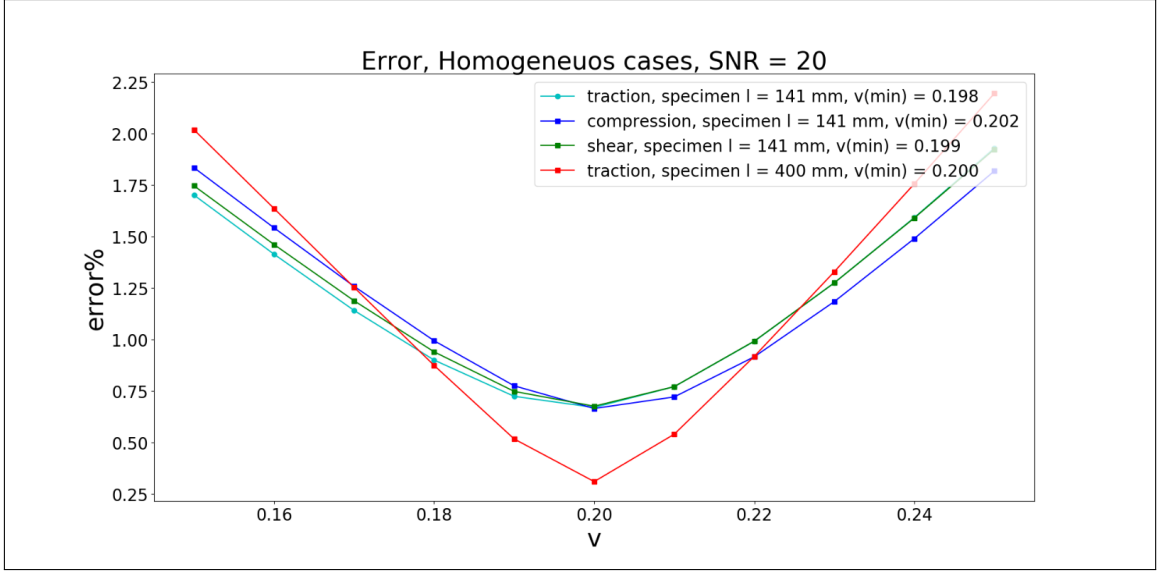


Figure 31: Identification homogeneous cases, different types of load and sample size.

Identification ν	different types of load and sample size
input	$\nu = 0.20$
traction, small	$\nu_{min} = 0.198$
compression	$\nu_{min} = 0.202$
"shear"	$\nu_{min} = 0.199$
traction, big	$\nu_{min} = 0.200$

Table 2: Identification homogeneous, material, different types of load and sample size.

For the homogeneous case the identification is always verified (for SNR values greater than 4).

4.2 Case with a large void spherical defect

Once the procedure for the homogeneous case is verified, is possible to proceed to the introduction of defects in the in the synthetic sample. As a first step, a single spherical defect is inserted. Features:

- cube side = 400 mm;
- correlation length = 3 mm;
- defects: central sphere, radius = 20, 50, 100 mm;
- SNR = 20;
- input parameters for FE simulations: $\nu=0.2$, $E = 10e3$ MPa;
- imposed deformation = +8.51 mm z direction (**traction**);

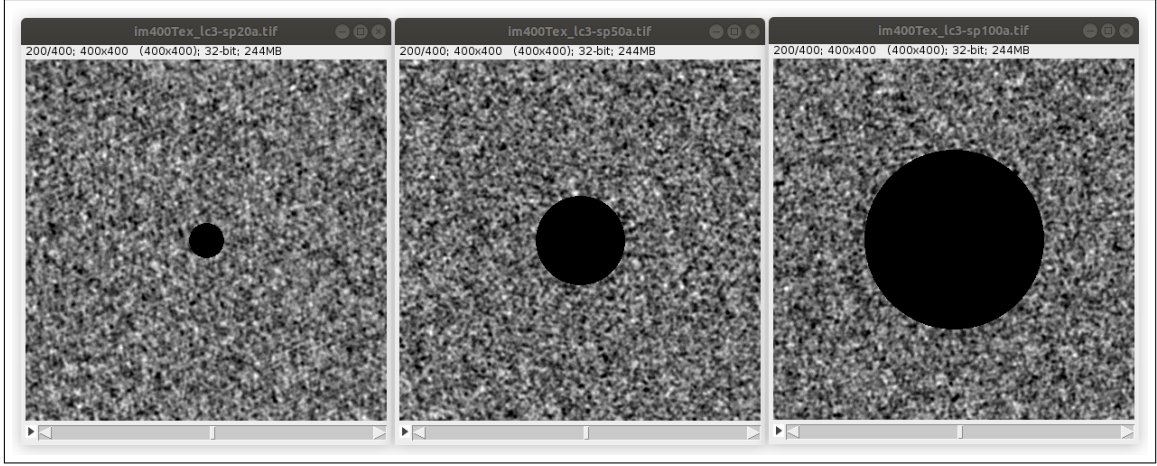


Figure 32: Cases with central sphere, $l = 400$ mm, $l_c = 3$ mm, radius = 20, 50, 100 mm.

At first it is useful to make a parametric analysis in order to find the characteristic length of the mesh that can well identify the defect and that does not require too much calculation time. To do this, a comparison of the macroscopic stress-strain response is done. A larger number of diameters are considered for this parametric analysis. Analysed case:

- $l_{char} = 5, 6, 10, 15$ mm;
- radius = [10, 120, 10] mm.

What is done is the extraction of the displacements and related forces from the tensile test simulations. Young's modulus and the stress-displacement graph are then obtained following the procedure explained in the chapter 2, Equation (9). Finally, it is possible to compare the $E_{macroscopic}$ obtained and the $E_{input} = 10e3$ MPa. Since the curves obtained are many, only one graph is reported, Figure 33.

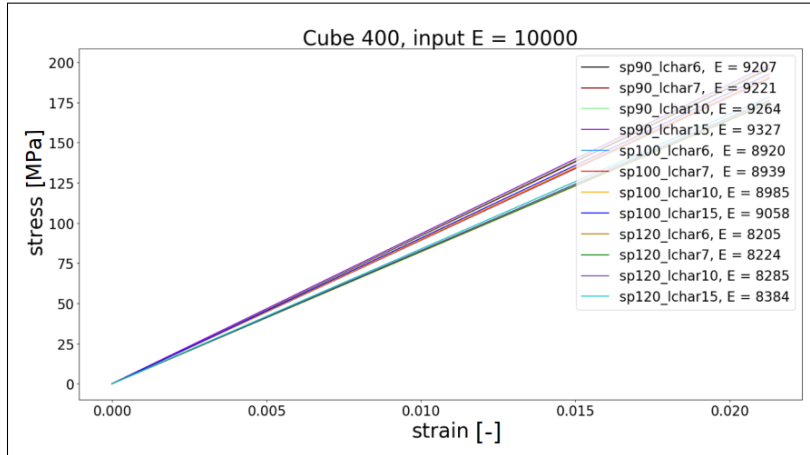


Figure 33: Macroscopic stress-strain response radius = 90, 100, 120 mm, $l_{char} = 5, 6, 10, 15$ mm.

In general the curves are very similar to each other. When radius = 10 mm is practically like the homogeneous case, it finds exactly the input E . Increasing the size of the sphere the 4 curves with the same sphere move away from each other, so l_{char} becomes more influential. The sphere is not well represented when l_{char} is bigger (Figure 34) with the result that Young macroscopic moduli found with coarse meshes are more dispersed.

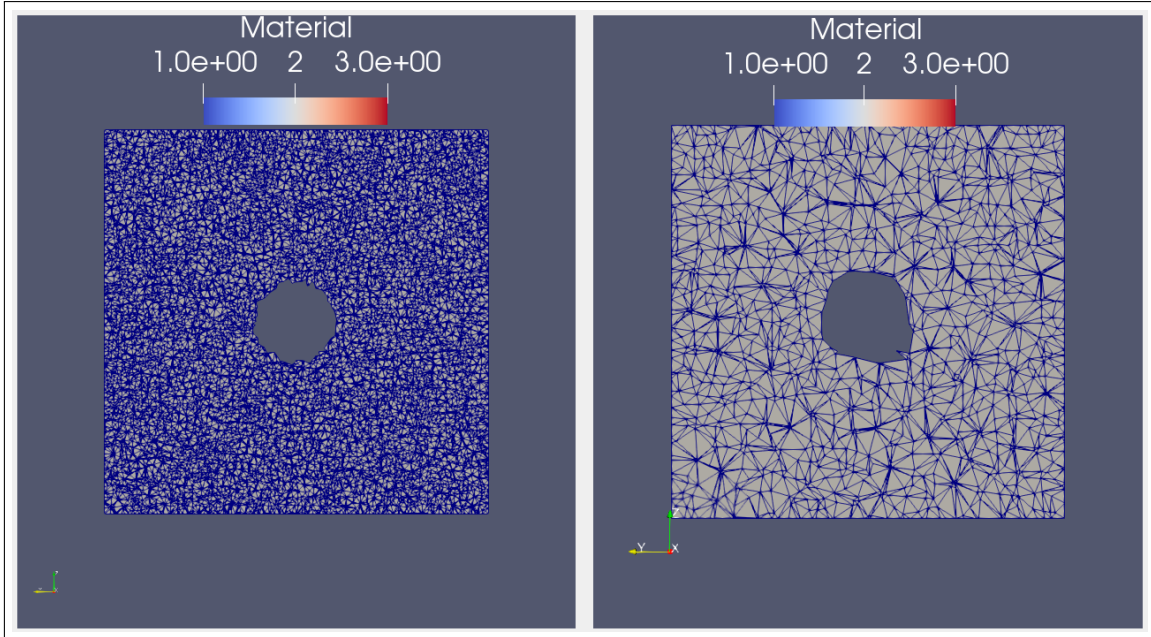


Figure 34: Difference in representation of a sphere of radius 40 mm between a mesh with $lchar = 6$ mm and $lchar = 15$ mm.

For the identification of the next cases is been used $lchar = 7$ mm because between 6 and 7 there is not a big difference (e.g. in the case $sp = 100$, $E_{(lchar=6)} = 8920$ MPa, $E_{(lchar=7)} = 8939$ MPa), but in terms of times $lchar = 7$ mm is quite faster.

Once the mesh to be used is chosen, the images of the deformed states can be obtained, Figure 35.

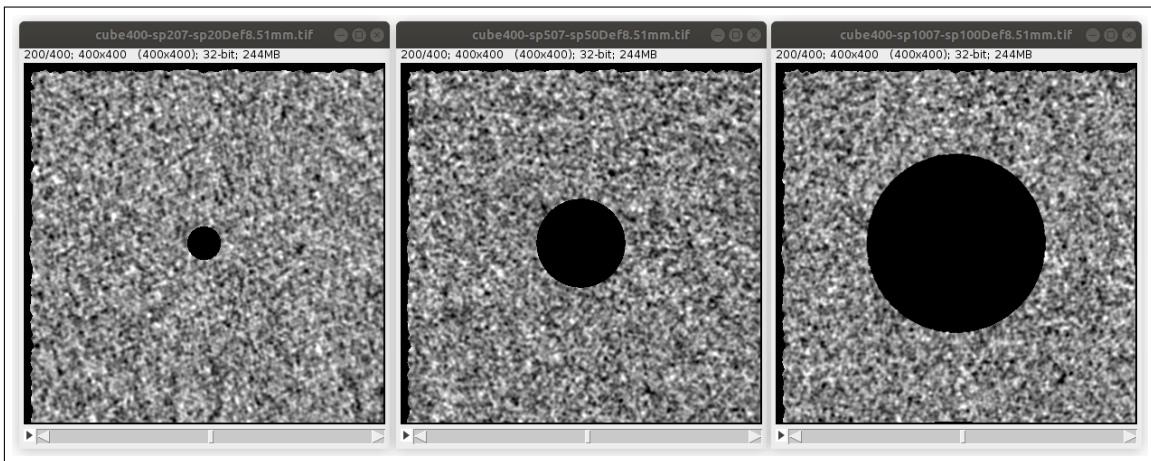


Figure 35: Cases with central sphere, $l = 400$ mm, $lc = 3$ mm, radius = 20, 50, 100 mm, $lchar = 7$ mm, deformed configuration.

At this point it is possible to continue with the step 3 (paragraph 4.1.3) starting from the DVC.

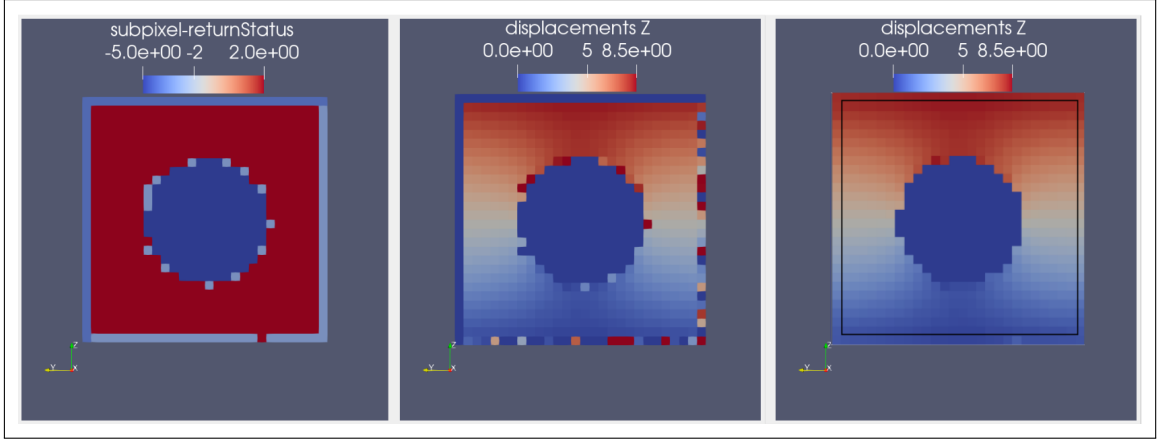


Figure 36: Cases with central sphere, $l = 400$ mm, $l_c = 3$ mm, radius = 100 mm, $l_{char} = 7$ mm, $h_{ws} = 7$ mm, return status and displacement in z direction from the DVC (b), displacement in z direction corrected (c).

As can be seen from Figure 36a, in this case the results are different from the homogeneous case. Since the defect has no texture in correspondence of the sphere it is not possible to reach convergence, a mask is set so that in correspondence of the defect the correlation does not even begin, the RS is equal to -5 and the displacements are set as NaN. In the representation, Figure 36b, such displacements are displayed as 0. From the DVC is also possible to notice that in correspondence of the sphere's edge some windows don't correlate, and the displacements associated with them are incorrect. It is possible to replace the displacements at $RS = -1$ with the average of the windows that were successfully correlated, thus obtaining the corrected DVC 36c.

Before interpolating towards the FE mesh, the borders of the displacement field are cropped, as in the homogeneous case.

The interpolated DVC, corrected and cropped, in the mesh of the initial configuration is shown in Figure 37.

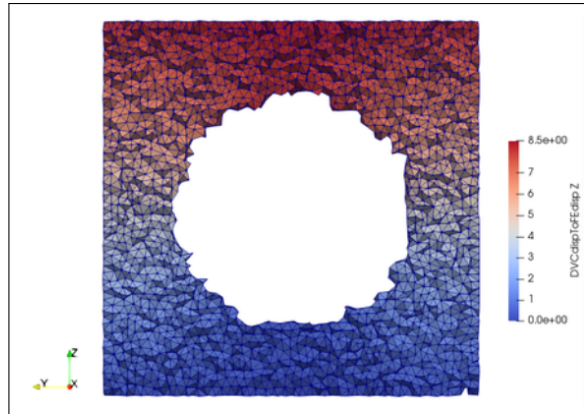


Figure 37: Interpolated DVC, cases with central sphere, $l = 400$ mm, $l_c = 3$ mm, radius = 100 mm, $l_{char} = 7$ mm, $h_{ws} = 7$ mm, displacement in z direction from the DVC corrected and interpolated.

To perform the simulations, the boundary conditions obtained from the displacement field in Figure 37 are imposed on a mesh where the nodes in correspondence of the void are deleted, the displacement fields obtained are of the type visible in Figure 38.

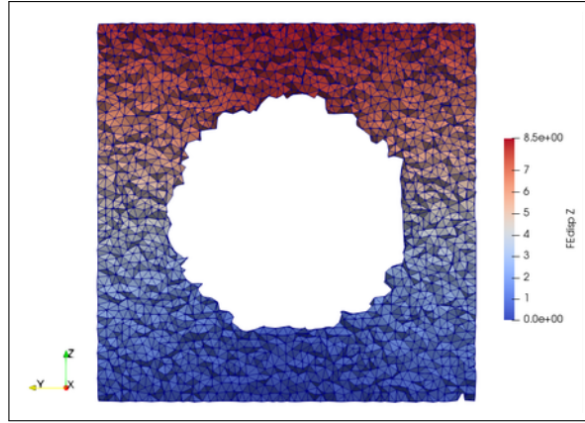


Figure 38: Cases with central sphere, $l = 400$ mm, $l_c = 3$ mm, radius = 100 mm, $l_{char} = 7$ mm, $h_{ws} = 7$ mm, displacement in z direction from the simulated displacement field.

As seen in Section 4.1.4 and 4.1.5, at this point the residuals (one of these is shown in the Figure 39) and the errors are determined.

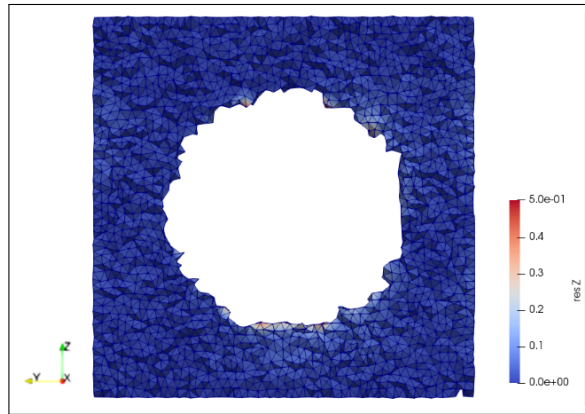


Figure 39: Cases with central sphere, $l = 400$ mm, $l_c = 3$ mm, radius = 100 mm, $l_{char} = 7$ mm, $h_{ws} = 7$ mm, residual field.

As for the homogeneous case, once checked the residual field the next step is the identification itself, see paragraph 4.1.5.

The results of the identification are visible in Figure 40 and more summarized in the table 3.

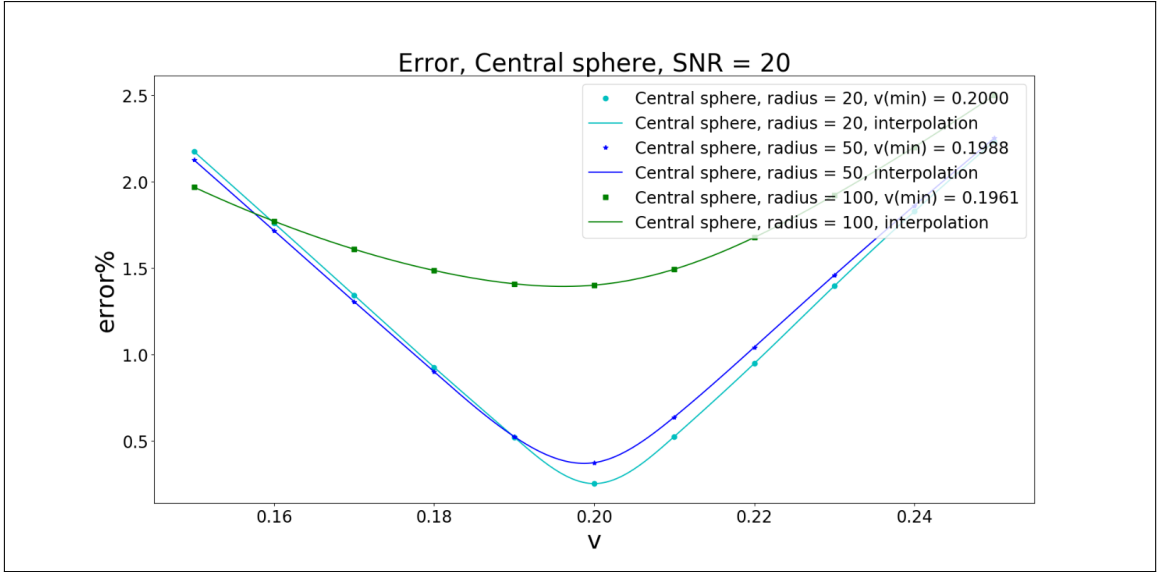


Figure 40: Cases with central sphere, $l = 400$ mm, $l_c = 3$ mm, radius = 100 mm, $l_{char} = 7$ mm, $h_{ws} = 7$ mm, minimisation of the error.

It is noticeable how, moving away from the homogeneous case, the interpolating curves are less convex, but the identification is always successful.

Identification v	different defect size
input	$v = 0.20$
radius = 20 mm	$v_{min} = 0.2000$
radius = 50 mm	$v_{min} = 0.1988$
radius = 100 mm	$v_{min} = 0.1961$

Table 3: Identification case with a large void spherical defect.

4.3 Case with many void spherical defects

4.3.1 Difference between working on the complete specimen and cropping around a single sphere

The first case treated is a cube of side 400 mm, with inside 6 spheres of radius 20 mm, a vertical section of this cube is visible in Figure 41a. It is interesting to try to understand if it might be possible to get Poisson's ratio by cropping around a single defect (Figure 41b), instead of considering the whole cube.

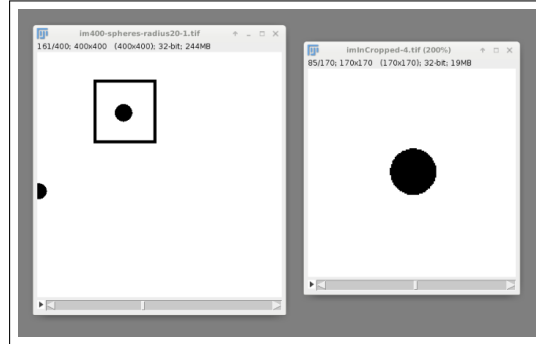


Figure 41: Cases with 6 spheres, $l = 400$ mm, radius = 20 mm, $l_{char} = 7$ mm, $h_{ws} = 7$ mm, initial configuration, whole sample and cutout around a sphere.

In both cases the value of Poisson's ratio is retrieve, as can be seen in Figure 45 and more summarized in the table 5.

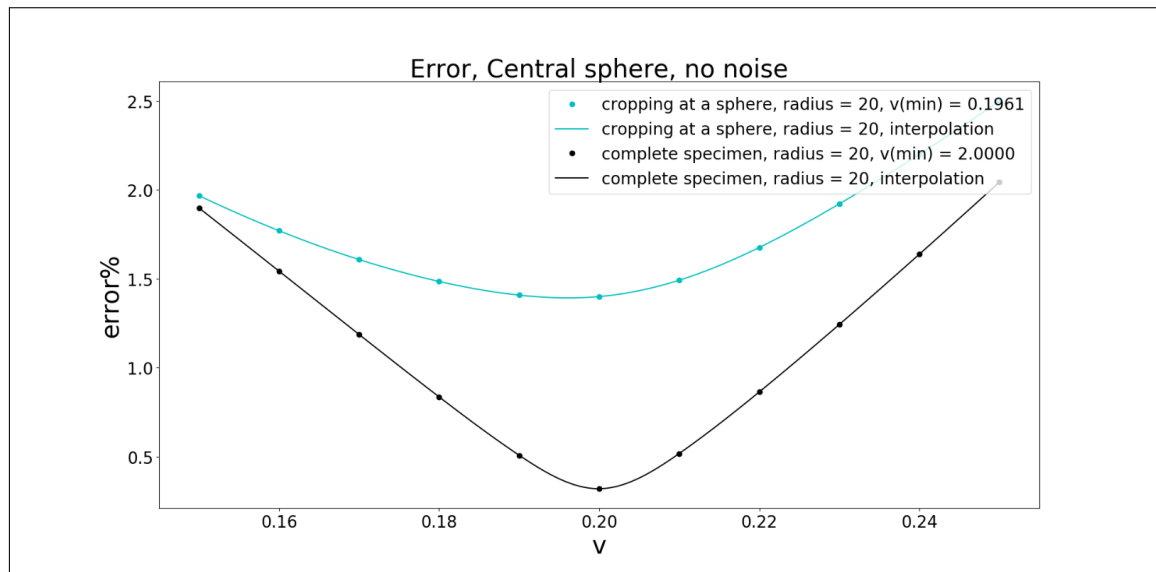


Figure 42: Cases with 6 spheres, $l = 400$ mm, radius = 20 mm, $l_{char} = 7$ mm, $h_{ws} = 7$ mm, minimisation of the error.

Identification v	different types of analysis
input	$v = 0.20$
whole sample	$v_{min} = 0.2000$
cutout around a sphere	$v_{min} = 0.1961$

Table 4: Identification case many void spherical defect, complete specimen and cropping around a single sphere.

4.3.2 Big number of defects

The last synthetic example foresees a cube of side 400 mm with inside a number of defects in order to have void ratio = 0.1, Equation (19).

$$e = \frac{V_V}{V_S} \quad (19)$$

V_V : volume of voids.

V_S : volume of solids.

Figure 43 shows one of the cubes, where the defects have a radius of 30 mm.

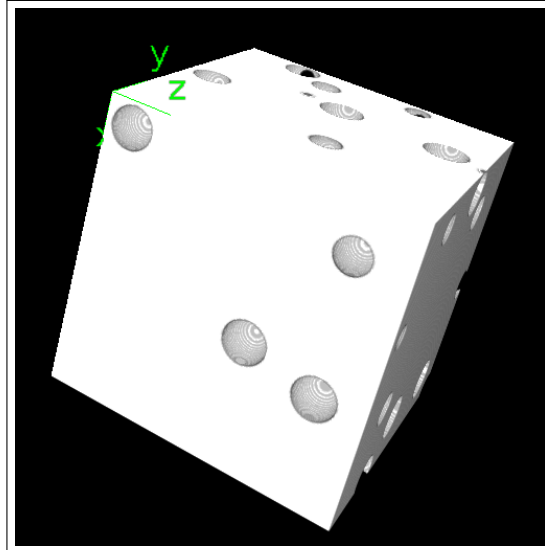


Figure 43: Cases with big number of defects, $l = 400$ mm, radius = 30 mm.

To decide the settings to be used, a parametric analysis is performed by trying:

- Radius = 30, 50, 100;
- $lc = 3, 5, 7, 9$;
- $lchar = 7$;
- $hws = 5, 7, 9, 11, 13$.

Using the complete procedure described in the Section 4.1.4, the parameter set that leads to the lowest error can be found, one of the error surfaces, in the homogeneous case are error curves. Figure 26, is shown visually below.

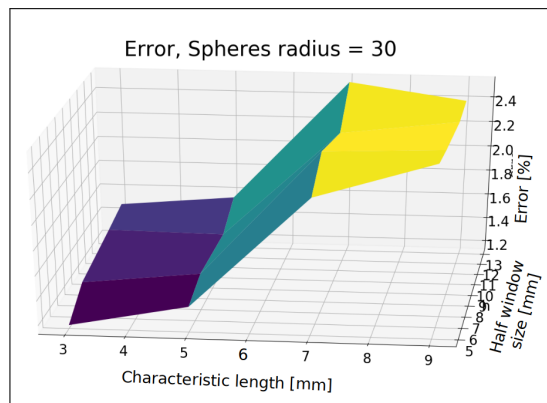


Figure 44: Cases with big number of defects, $l = 400$ mm, radius = 30 mm, parametric analysis.

As can be seen from the graph, the configuration that leads to the smallest error for 30 mm radius spheres is:

- Spheres 30 mm: $lc = 3$, $hws = 5$;

Similarly for the other cases it is found:

- Spheres 50 mm: $lc = 5$, $hws = 11$;
- Spheres 100 mm: $lc = 7$, $hws = 13$;

At this point the identification process is carried out, obtaining also in this case the Poisson's ratio, as seen in in Figure 45 and more summarized in the table 5.

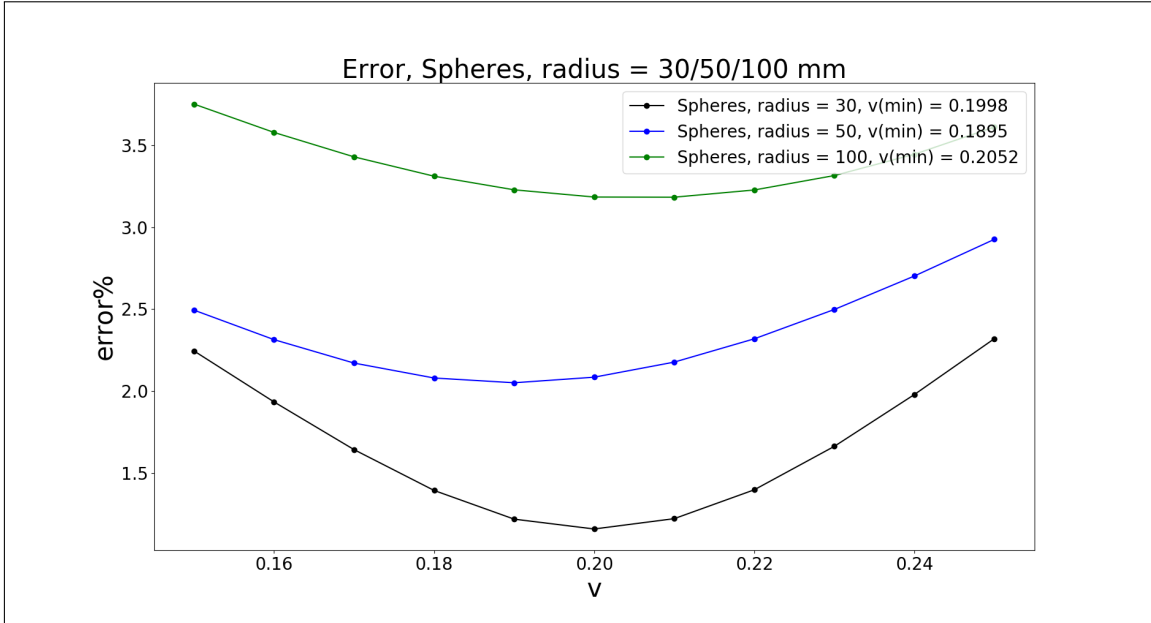


Figure 45: Cases with big number of defects, $l = 400$ mm, radius = 30/50/100 mm, minimisation of the error.

Identification v	different spheres size
input	$v = 0.20$
radius = 30 mm	$v_{min} = 0.1998$
radius = 50 mm	$v_{min} = 0.1895$
radius = 100 mm	$v_{min} = 0.2052$

Table 5: Identification case many void spherical defect, different spheres size.

5 Experimental kinematic fields

In chapter 4.1 is explained the whole procedure for the identification of Poisson's ratio in case the initial and final configuration are simulated, when instead it is possible to obtain them through x-ray computed tomography what changes in the flowchart in Figure 9 are only Step 1 and Step 2.

The Experimental campaign consists in a uniaxial compression test (with imposed deformation and force measurement), in which, after each load step, the 3D image of the specimen is acquired through the tomograph.

In chapter 3.1 is explain how the image of the initial configuration (Step 1) and of the deformed configuration (Step 2) are generated by the reconstruction of the scans.

5.0.1 Material

The first step for this experimental campaign is the research of the materials to be tested. Since the work is limited to the elastic theory the materials selected had to be elastic, and in order to correctly measure the forces exerted during the compression test the material had to be sufficiently rigid. Moreover, in order to guarantee the functioning of the correlation it had to have a texture that could be seen in the images.

Trying to follow these criteria, a pool foam noodle made of expanded polyethylene and a cellulose sponge are chosen.

For the foam noodle 3 different specimens are made, shown in Figure 46, all cylindrical with size ratio 1/2, diameter = 50 mm, height = 100 mm.

- NFH: noodle foam homogeneous;
- NFD: noodle foam with a defect, cylindrical void with axis perpendicular to the axis of the sample;
- NFDBC: noodle foam with a defect, cylindrical void with axis perpendicular and also unfavourable boundary conditions.

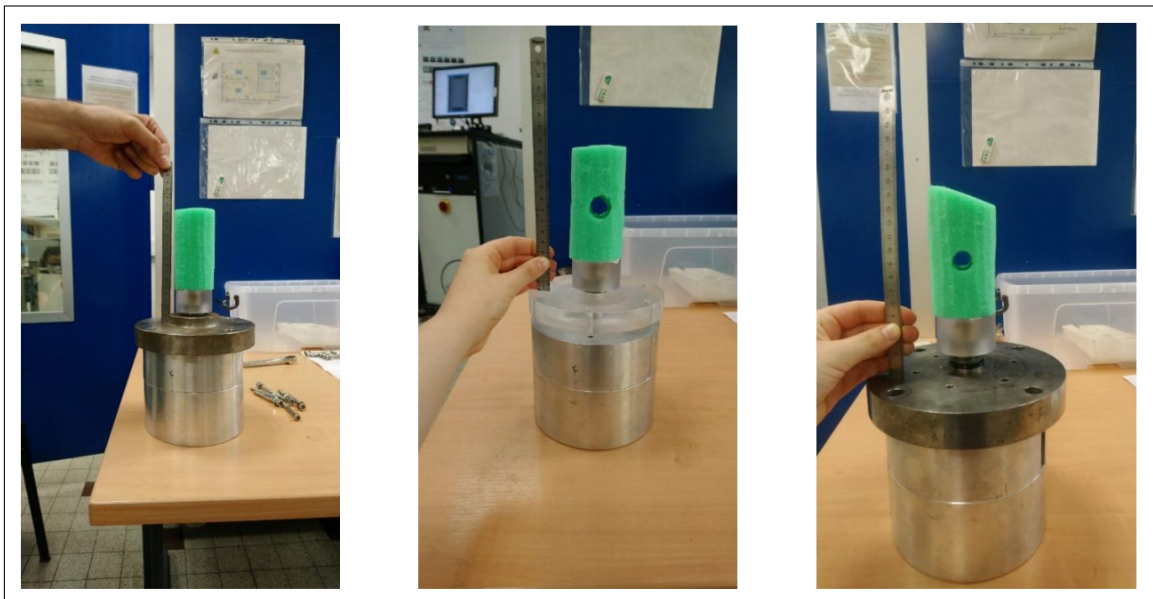


Figure 46: Noodle foam, Sample 1, 2 and 3, respectively, homogeneous, with defect, with defect and bad boundary conditions.

For the sponge, Figure 47, a cylindrical specimen with a 40 mm side is made.



Figure 47: Sponge sample.

These samples recall the cases analyzed in the Section 4.1, 4.2 and 4.3.2: Homogeneous, One large defect, Big number of defects.

5.0.2 In-situ experiments

Noodle Foam For the three case of the NF the voltage and current of the x-ray source are set to 100 kV and 500 μ A, and the voxel size is set to 68 μ m. Projections are acquired in 1120 different angular positions between 0 and 360.

NFH

For the first sample eight scans are performed. Figure 48 show the experimental macroscopic force-displacement curve the experiments. The loading steps where the tomographic scans are carried out are indicated.

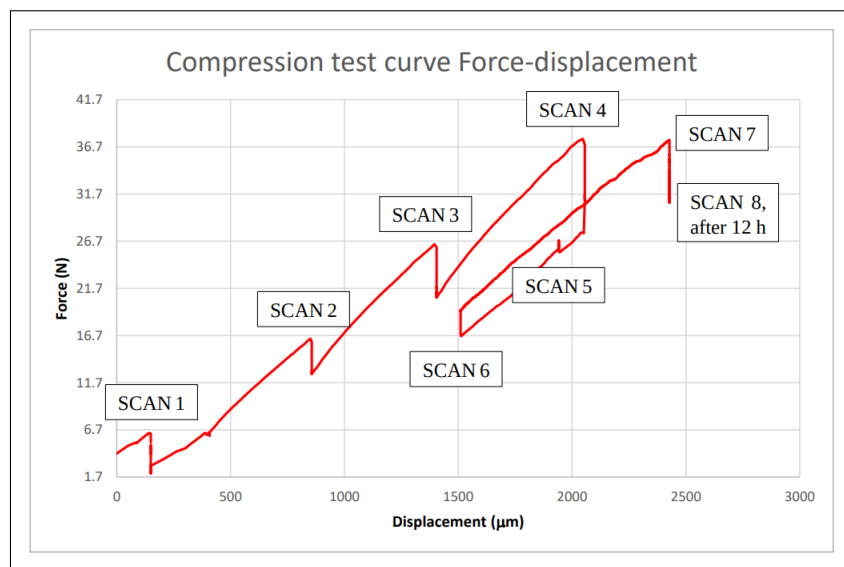


Figure 48: Noodle foam, Sample 1 macroscopic force-displacement curve.

NFD

For the second sample three scans are performed. Figure 49 show the experimental macroscopic force-displacement curve the experiments. The loading steps where the tomographic scans are carried out are indicated.

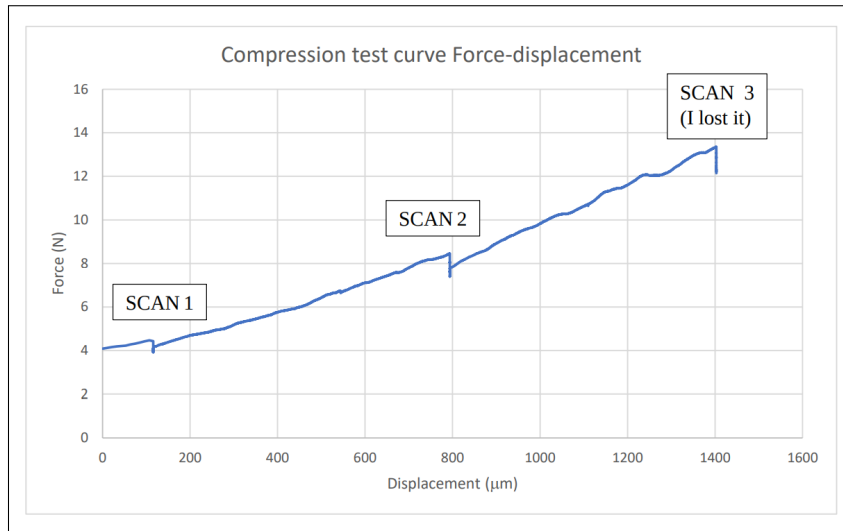


Figure 49: Noodle foam, Sample 2 macroscopic force-displacement curve.

NFDBC

For the third sample three scans are performed. Figure 50 show the experimental macroscopic force-displacement curve the experiments. The loading steps where the tomographic scans are carried out are indicated.

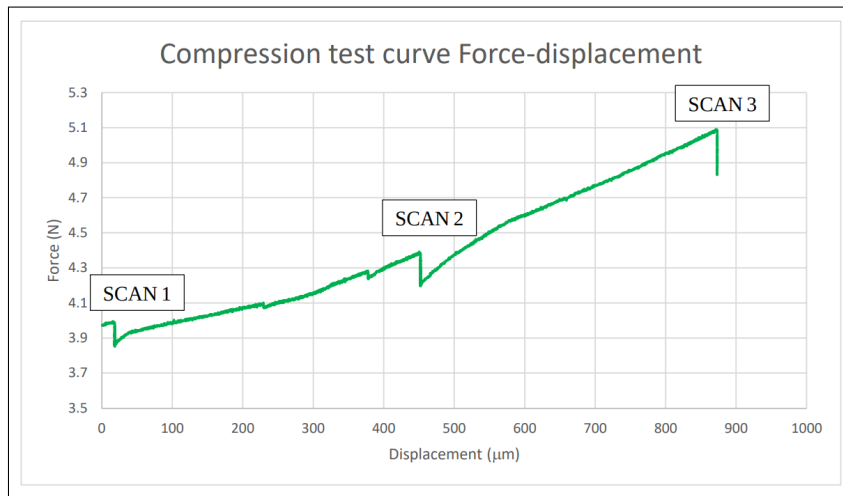


Figure 50: Noodle foam, Sample 3 macroscopic force-displacement curve.

Sponge For the three case of the NF the voltage and current of the x-ray source are set to 100 kV and 300 μ A, and the voxel size is set to 43 μ m. Projections are acquired in 1120 different angular positions between 0 and 360. For the sponge three scans are performed. Figure 51 show the experimental macroscopic force-displacement curve the experiments. The loading steps where the tomographic scans are carried out are indicated.

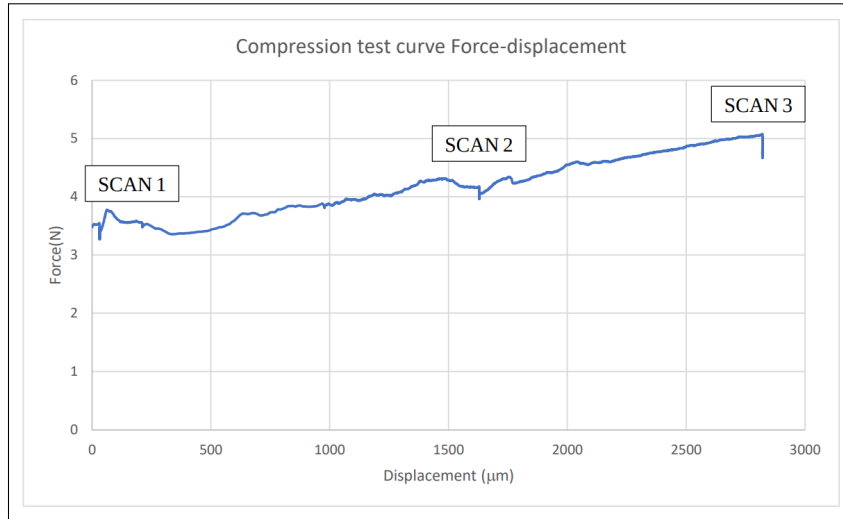


Figure 51: Sponge, macroscopic force-displacement curve.

Macroscopic Young's modulus

From the force-displacement information is possible to derive macroscopic Young's module, following the Equation (9) in chapter 2:

- Pool Noodle (from sample 1) $E_{macroscopic} \simeq 1$ MPa;
- Sponge $E_{macroscopic} \simeq 0.01$ MPa.

By assembling the 2D radiographs using a filtered back projection algorithm available in the XAct software (provided by RX-Solutions, Annecy, France), the reconstructed 3D image of the scanned specimen is obtained.

The Figures 52 and 53 show the central horizontal and vertical slices of first scans (where the specimens are at rest), respectively for NFH, NFD, NFDBC and for the sponge.

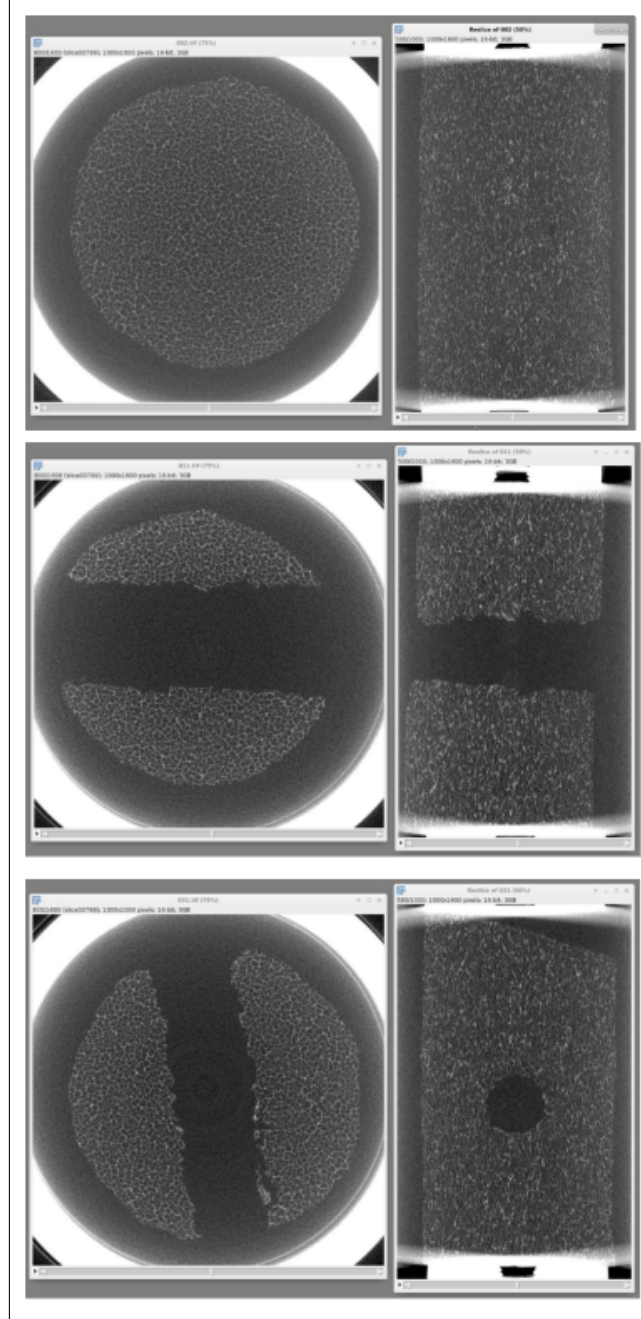


Figure 52: Central horizontal and vertical slices of the reconstructed 3D images of the SCAN 1, Noodle foam, respectively, NFH, NFD, NFDBC.

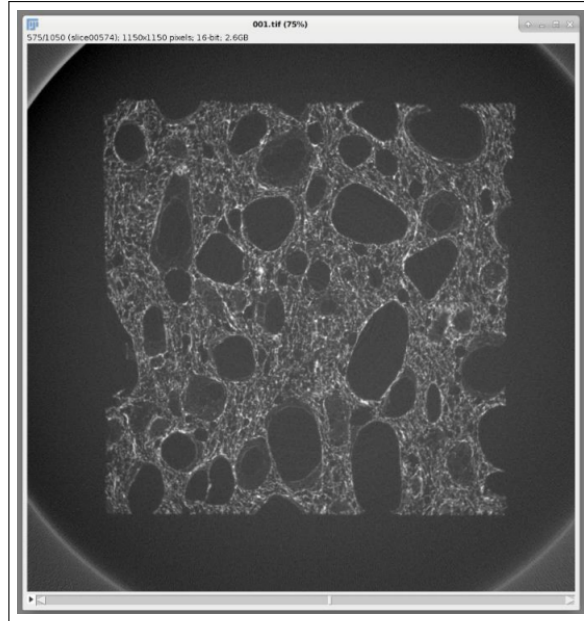


Figure 53: Central vertical slices of the reconstructed 3D images of the SCAN 1, Sponge.

5.1 Step 3: Local Digital Image Correlation, Extracting the boundary conditions

As in the paragraph 4.1.3, once the images of the initial configuration and the deformed configuration are obtained, it is possible to continue with the LDIC.

In the real case during the test the sample is also subjected to rigid body motion, this has been automatically subtracted by Spam during the correlation.

As in simulated cases, when the sample is homogeneous the DVC has no windows that do not correlate, if away from the edges, the result is a smooth displacement field.

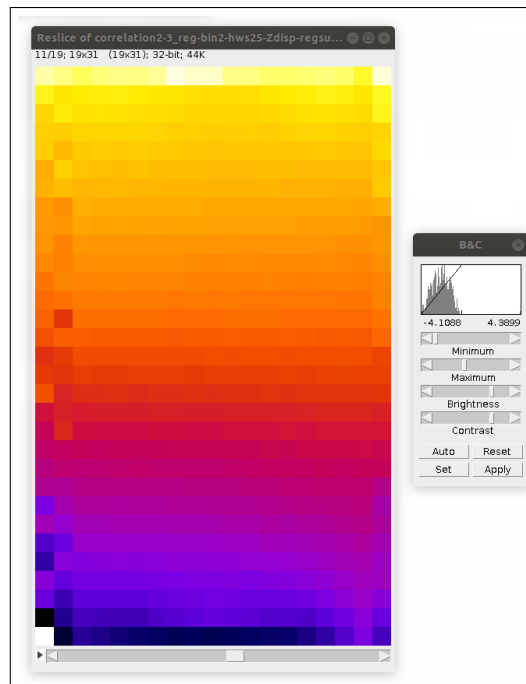


Figure 54: NFH, results from LDIC Scan2-Scan3, axial displacement field, hws = 25 px.

On the other hand, if the defect is present, there are windows that do not correlate:

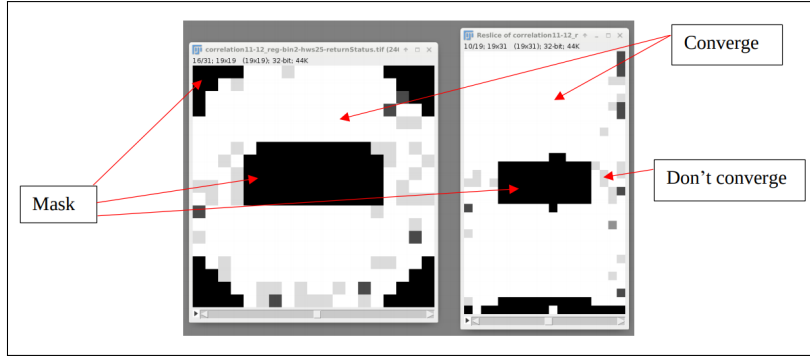


Figure 55: NFD, results from LDIC Scan1-Scan2, return status, hws = 25 px.

It is possible to replace the displacements at RS = -1 with the average of the displacements surrounding the windows in consideration, thus obtaining the correct DVC, as seen in paragraph 4.2.

From the DVC is possible to obtain Young's modulus form and Poisson's ratio, σ_{zz} is calculated in the classical way, using force and area, Equation (9), the longitudinal strains are found from the displacement field in which Δl can be obtained in pixels.

- Pool Noodle (from sample 1) $E_{DVC} \simeq 1.34 \text{ MPa}/ v_{DVC} \simeq 0.44$.
- Sponge $E_{DVC} \simeq 0.016 \text{ MPa}$.

The rest of the procedure is analogous to the simulated case, the mesh is created from the cropped initial configuration (Figure 56a) and then the cropped DVC is interpolated in the mesh as shown in Figure 56 b.

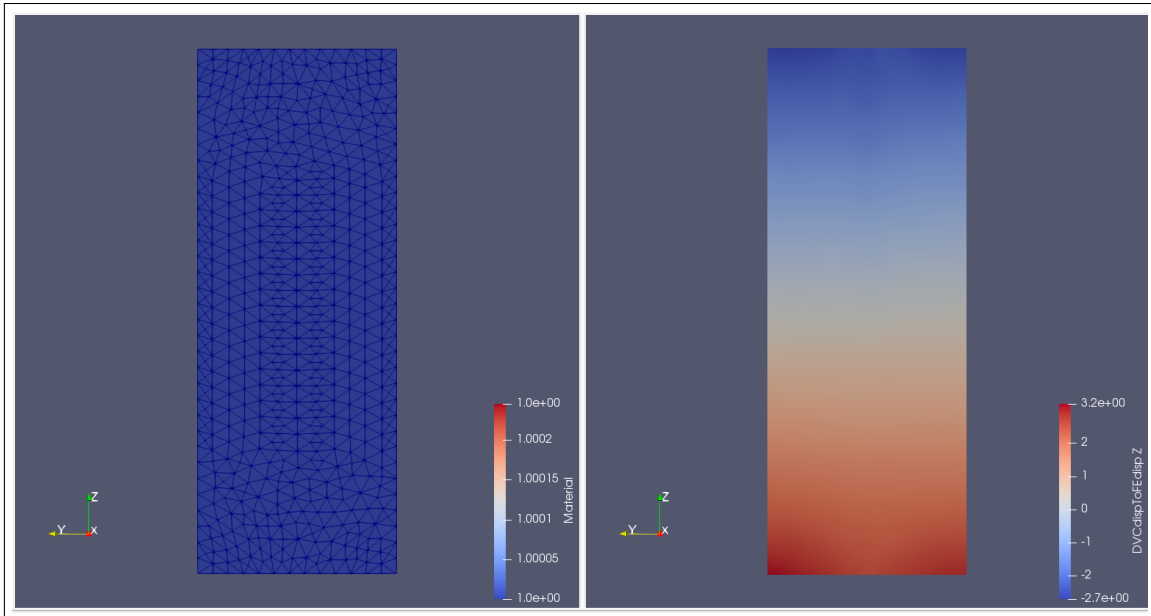


Figure 56: NPH, mesh of the initial configuration, and DVC interpolated in the mesh.

5.2 Step 4: Identification of elastic parameters

5.2.1 NPH

The boundary conditions are extracted from 56 b and simulations with different Poisson's ratios are carried out. One of the displacement fields (obtained for $\nu = 0.40$) with the residual is shown in Figure 57, where (a) is the interpolated DVC field, (b) is the simulated field and (c) is the residual.

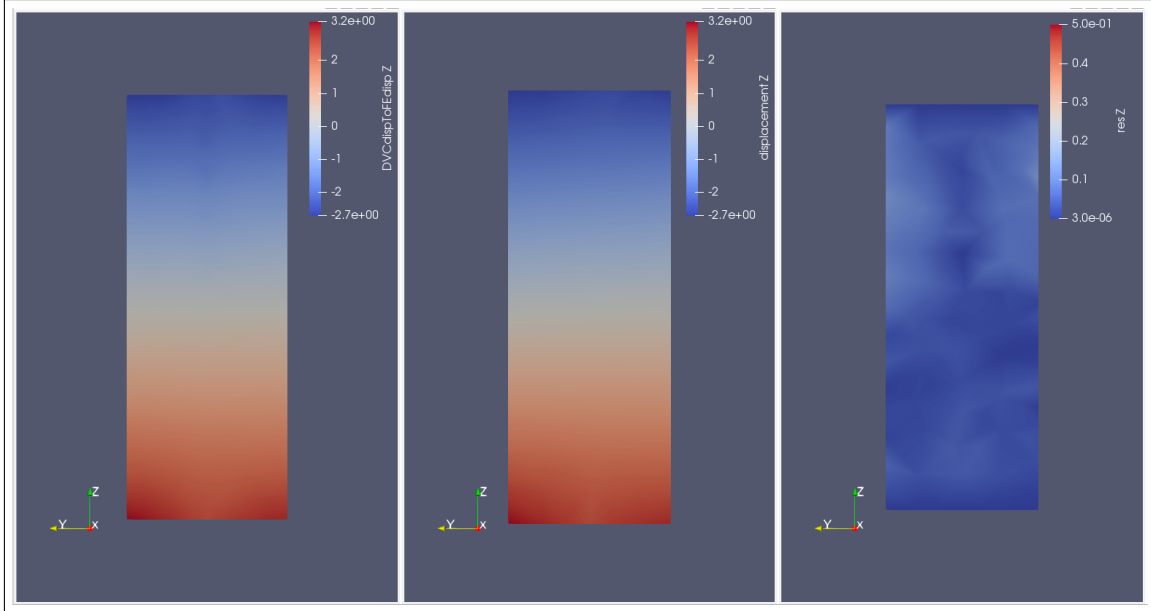


Figure 57: NPH axial displacement field DVC interpolated in the mesh, axial displacement field simulated, residual z direction.

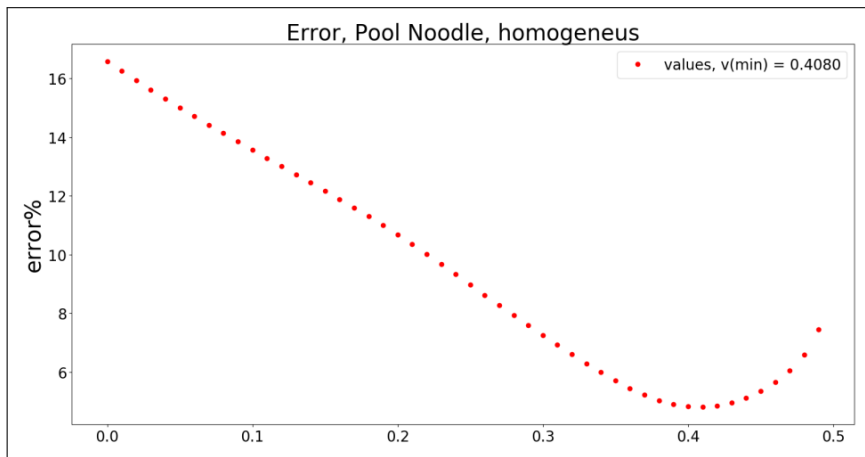


Figure 58: NPH, minimisation of the error.

As can be seen from Figure 58, in which the error minimisation is displayed, the value found for Poisson's ratio is $\nu_{min} = 0.4080$.

5.2.2 Noodle foam, heterogeneous, Sponge

For the remaining samples the procedure is not successful, it is not possible to find a minimum of the interpolating function of the error values.

There may be a number of reasons why it is not possible to make the identification. Since the materials are not rigid enough the displacements applied are very modest, this could have caused the information from the DVC to have the same order of magnitude as the noise.

6 Conclusions and Perspectives

In chapter 4 it has been demonstrated how the combination of full field measurements and finite element simulations allows the very precise identification of Poisson's ratio, when images are simulated. Identification is also possible in case the noise level in the images is very high (so much to be in realistic) bringing the procedure to break only for SNR values less than 8 (an SNR = 10 is considered acceptable).

On the contrary, in the case of real images, obtained with a tomograph, it has been possible to identify Poisson's ratio only in the homogeneous case, for which, in general, conventional material tests are enough to find the elastic parameters.

To complete the discussion, at simulated level it would be interesting to insert in the initial configuration some defects that are not empty, but that are a second material, so that it would be possible to attempt the identification also for the ratio between Young's moduli.

As far as the experimental part is concerned, testing a more rigid elastic material, thus being able to impose greater deformations could be a solution.

References

- spam's documentation. URL <https://ttk.gricad-pages.univ-grenoble-alpes.fr/spam/index.html>.
- L. Babout. X-ray image a necessary tool for material science. 2006.
- H. Bui. Sur quelques problèmes inverses élastiques en mécanique de l'endommagement. In *Deuxième colloque national de calcul des structures*, pages 26–35, 1995.
- A. Buljac, C. Jailin, A. Mendoza, J. Neggens, T. Taillandier-Thomas, A. Bouterf, B. Smaniotto, F. Hild, and S. Roux. Digital volume correlation: review of progress and challenges. *Experimental Mechanics*, 58(5):661–708, 2018.
- D. Claire, F. Hild, and S. Roux. A finite element formulation to identify damage fields: the equilibrium gap method. *International journal for numerical methods in engineering*, 61(2):189–208, 2004.
- M. Grediac. The use of full-field measurement methods in composite material characterization: interest and limitations. *Composites Part A: applied science and manufacturing*, 35(7-8):751–761, 2004.
- M. Grédiac and F. Hild. *Full-field measurements and identification in solid mechanics*. John Wiley & Sons, 2012.
- F. Hild and S. Roux. Comparison of local and global approaches to digital image correlation. *Experimental Mechanics*, 52(9):1503–1519, 2012.
- K. T. Kavanagh and R. W. Clough. Finite element applications in the characterization of elastic solids. *International Journal of Solids and Structures*, 7(1):11–23, 1971.
- P. Ladeveze and D. Leguillon. Error estimate procedure in the finite element method and applications. *SIAM Journal on Numerical Analysis*, 20(3):485–509, 1983.
- R. Lancellotta. *Geotechnical engineering*. CRC Press, 2008.
- B. D. Lucas, T. Kanade, et al. An iterative image registration technique with an application to stereo vision. 1981.
- E. Maire and P. J. Withers. Quantitative x-ray tomography. *International materials reviews*, 59(1):1–43, 2014.
- E. Maire, P. Colombo, J. Adrien, L. Babout, and L. Biasetto. Characterization of the morphology of cellular ceramics by 3d image processing of x-ray tomography. *Journal of the European Ceramic Society*, 27(4):1973–1981, 2007.
- R. Rieger, J.-C. Aurgan, and T. Hoc. Micro-finite-element method to assess elastic properties of trabecular bone at micro-and macroscopic level. *Morphologie*, 102(336):12–20, 2018.
- L. Salvo, M. Suéry, A. Marmottant, N. Limodin, and D. Bernard. 3d imaging in material science: Application of x-ray tomography. *Comptes Rendus Physique*, 11(9-10):641–649, 2010.
- O. Stamati. *Effet des hétérogénéités sur le comportement mécanique du béton à l'échelle mésoscopique: apports de la micro-tomographie à rayons-x in-situ combinée à une modélisation E-FEM*. Thèse, Université Grenoble Alpes, 2020.
- O. Stamati, E. Andò, E. Roubin, and C. R. et al. spam: Software for practical analysis of materials. *Submitted to Journal of Open Source Software*, 5(50):2177, 2020.
- R. L. Taylor. Feap-a finite element analysis program, 2014.
- E. Tudisco, C. Jailin, A. Mendoza, A. Tengattini, E. Andò, S. A. Hall, G. Viggiani, F. Hild, and S. Roux. An extension of digital volume correlation for multimodality image registration. *Measurement Science and Technology*, 28(9):095401, 2017.

- C. Veyhl, I. Belova, G. Murch, and T. Fiedler. Finite element analysis of the mechanical properties of cellular aluminium based on micro-computed tomography. *Materials Science and Engineering: A*, 528(13-14):4550–4555, 2011.
- G. Viggiani and S. A. Hall. Full-field measurements, a new tool for laboratory experimental geomechanics. In *Fourth symposium on deformation characteristics of geomaterials*, volume 1, pages 3–26. IOS Press Amsterdam, 2008.

Chiara Rossi

Civil Engineer

via Nardelli, 34
Porto Azzurro (LI), 57036 Italy
☎ 328 - 211 69 82
✉ chiara.rossi@3sr-grenoble.fr



Education

- Feb 2020–up to present **Internship aimed at writing the master's thesis**, *Thesis: "Identification of elastic material parameters from (experimental) kinematic fields"*, Universite Grenoble Alpes (UGA), Grenoble, France.
- Sep 2019–up to present **E+/EU PROGRAMME COUNTRIES**, *Master in Geomechanics, Civil Engineering and Risks (GCER)*, Universite Grenoble Alpes (UGA), Grenoble, France.
- Sep 2018–up to present **Master's Degree in Civil Engineering (Geotechnics branch)**, *Politecnico di Torino*, Torino, [...].
- Sep 2014–Sep 2018 **Bachelor's Degree in Civil Engineering**, *Thesis: "Design of an inflection clothoid"*, Politecnico di Torino, Torino.
[99/110]
- Sep 2009–Jun 2014 **Scientific High School Diploma**, *Istituto Statale Istruzione Superiore R. Foresi*, Portoferraio, [86/100].

Professional Experiences

- 2015–up to present **Post-School Tutoring**,
Porto Azzurro – Turin,
Individual tutoring lessons in Mathematics and Physics.
- 2011–2014 **Camping Da Mario (family activity) – Secretary**,
Porto Azzurro,
Booking management and customer reception.

Computer Skills

- Languages Python, Matlab, C, L^AT_EX
- Operating Systems *Microsoft Windows, Linux*
- Programs *Software for the Practical Analysis of Materials SPAM, Autodesk AutoCAD, QGis, MathWorks Matlab, MicroSurvey Starnet, Microsoft Office*
- Certifications *2013 – European Computer Driving License (ECDL)*

Languages and others

- Languages Italian (Native Speaker), English (2017 – IELTS, Listening: 6.0, Reading: 7.5, Writing: 5.0, Speaking: 5.5, Overall: 6.0), French (basic knowledge)
- Driving License Italian Driving License class "B"